We are IntechOpen, the world's leading publisher of Open Access books Built by scientists, for scientists

6,900
Open access books available

185,000
International authors and editors

200M
Downloads

Our authors are among the

154
Countries delivered to

TOP 1%
most cited scientists

12.2%
Contributors from top 500 universities



WEB OF SCIENCE™

Selection of our books indexed in the Book Citation Index in Web of Science™ Core Collection (BKCI)

Interested in publishing with us?
Contact book.department@intechopen.com

Numbers displayed above are based on latest data collected.
For more information visit www.intechopen.com



16

Microstrip Antennas for Indoor Wireless Dynamic Environments

Mohamed Elhefnawy and Widad Ismail
Universiti Sains Malaysia (USM), Malaysia

1. Introduction

This chapter is organized in two parts. The first part deals with the design and implementation of a microstrip antenna array with Butler matrix. The planar microstrip antenna array has four beams at four different directions, circular polarization diversity, good axial ratio, high gain, and wide bandwidth by implementing the 4×4 Butler matrix as a feeding network to the 2×2 planar microstrip antenna array. The circular polarization diversity is generated by rotating the linearly polarized identical elements of the planar microstrip antenna array so that the E-field in the x-direction is equal to the E-field in the y-direction. Then, by feeding the planar array with Butler matrix, phase delay of $\pm\pi/2$ between those two E-fields is provided.

In the second part of this chapter, the analysis, design and implementation of an Aperture Coupled Micro-Strip Antenna (ACMSA) are introduced. A quadrature hybrid is used as a feeder for providing simultaneous circular polarization diversity with a microstrip antenna; but the utilization of the quadrature hybrid as a feeder results in large antenna size. In order to minimize the antenna size, the microstrip antenna is fed by a quadrature hybrid through two orthogonal apertures whose position is determined based on a cavity model theory. The size of the proposed ACMSA is small due to the use of the aperture coupled structure. The cavity model theory is started with Maxwell's equations, followed by the solution of the homogeneous wave equations. Finally, the eigenfunction expansion for the calculation of the input impedance is presented. This chapter is organized as follows. The first part deals with design and implementation of a microstrip antenna array with Butler matrix, which describe the design details of a rectangular microstrip patch antenna and a 4×4 Butler matrix. Further, analysis of planar microstrip antenna array with Butler matrix and the development of the radiation pattern for the planar microstrip antenna array are presented.

In the second part, the design and implementation of an aperture coupled microstrip antenna, the analysis of ACMSA using cavity model, the circular polarization diversity with ACMSA and the geometry of the ACMSA are described.

2. Design and implementation of the microstrip antenna array with Butler matrix

A planar microstrip antenna array with a Butler matrix is implemented to form a microstrip antenna array that has narrow beamwidth, circular polarization and polarization diversity.

This microstrip antenna array improves the system performance in indoor wireless dynamic environments. A circularly polarized microstrip antenna array is designed such that it consists of four identical linearly polarized patches. A 2×2 planar microstrip antenna array and a 4×4 Butler matrix are designed and simulated using advanced design system and Matlab software. The measured results show that a combination of a planar microstrip antenna array and a 4×4 Butler matrix creates four beams two of which have RHCP and the other two have LHCP.

2.1 Design of the rectangular microstrip patch antenna

A rectangular microstrip patch antenna is designed based on the Transmission Line Model (TLM) in which the rectangular microstrip patch antenna is considered as a very wide transmission line terminated by radiation impedance. Figure 1 shows a rectangular microstrip patch antenna of length L and width W. M_s is the magnetic current of each radiating slot of the microstrip patch antenna and s is the width of each radiating slot.

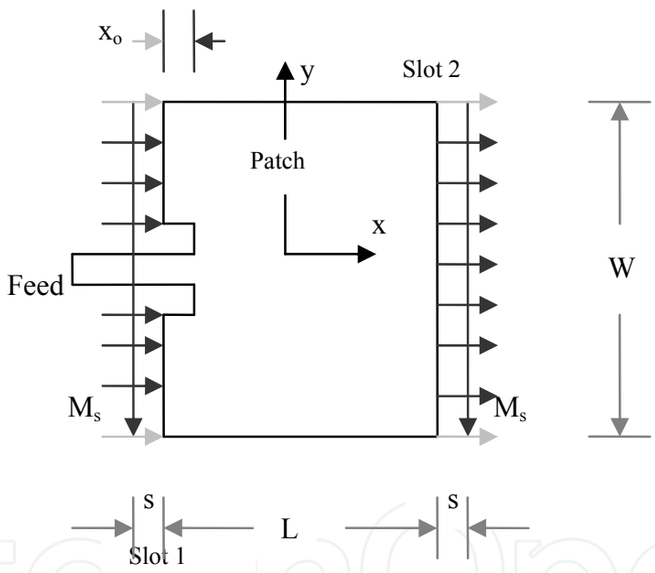


Fig. 1. Inset fed rectangular microstrip patch antenna

Figure 2 shows the transmission line model of the antenna where G_R and C_F represent the radiation losses and fringing effects respectively. The input impedance of an inset fed rectangular microstrip patch antenna is given by the equation (1) [1].

$$Z_{in} = \frac{1}{2\left(G_R + G_{12}\right)} \cos^2\left(\frac{\pi\ x_o}{L}\right) \tag{1}$$

where X_o is the distance into the patch, G_{12} is the coupled conductance between the radiating slots of the antenna [2].

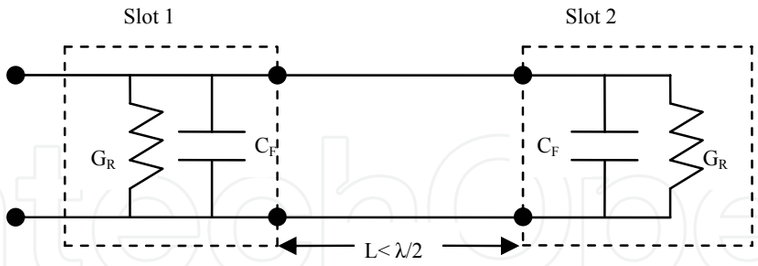


Fig. 2. Transmission line model of the rectangular microstrip patch antenna

The inset fed rectangular microstrip patch antenna is designed using Matlab software based on the expression for the input impedance which is given by equation (1). The input impedance depends on the microstrip line feed position as shown in Figure 3.

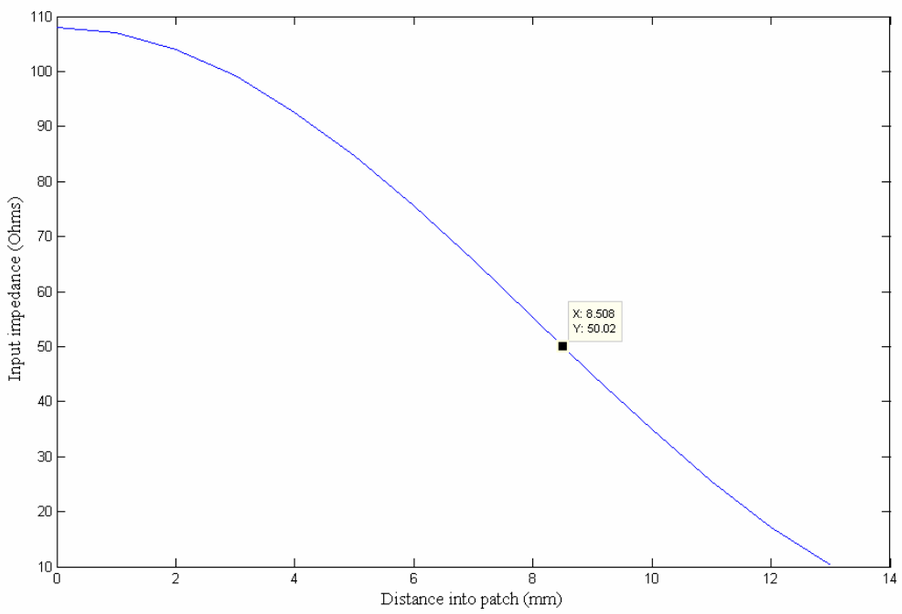


Fig. 3. Dependence of the input impedance on the distance into the patch

2.2 Design of the 4×4 Butler matrix

The Butler matrix is used as a feeding network to the microstrip antenna array and it works equally well in receive and transmit modes. The 4×4 Butler matrix as shown in Figure 4 consists of 4 inputs, 4 outputs, 4 hybrids, 1 crossover to isolate the cross-lines in the planar layout and some phase shifters [3]. Each input of the 4×4 Butler matrix inputs produces a different set of 4 orthogonal phases; each set used as an input for the four element antenna array creates a beam with a different direction. The switching between the four Butler inputs changes the direction of the microstrip antenna array beam.

Advanced design system (ADS) has been used for simulating the 4×4 Butler matrix as shown in Figure 5. Table 1 shows a summary of the simulated and the measured phases that are associated with the selected port of the 4×4 Butler matrix.

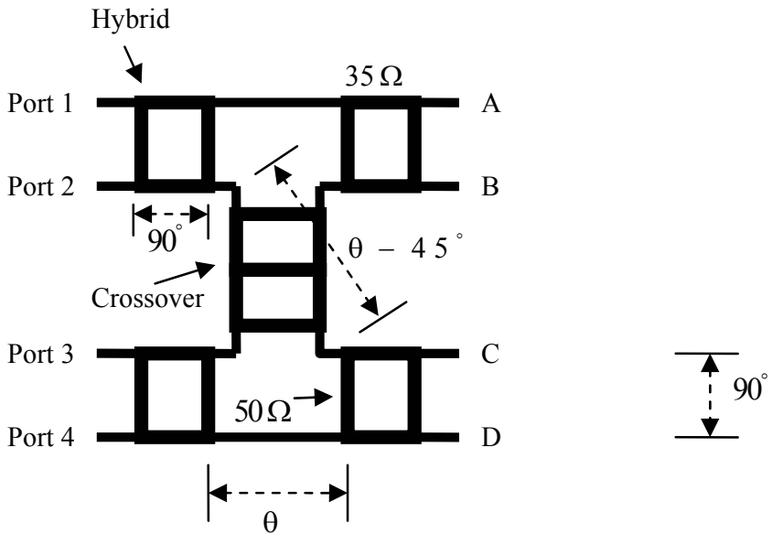


Fig. 4. 4×4 Butler matrix geometry

		Phase A Antenna 1	Phase B Antenna 2	Phase C Antenna 3	Phase D Antenna 4
Port 1 **(set 1)**	**Theoretical**	0	-90	-45	-135
	Simulated	0	-89.813	-45.04	-135.04
	Measured	0	-98	-50	-142.8
Port 2 **(set 2)**	**Theoretical**	0	-90	135	45
	Simulated	0	-90.273	134.142	44.773
	Measured	0	-80.5	140.5	48.5
Port 3 **(set 3)**	**Theoretical**	0	90	-135	-45
	Simulated	0	89.369	-135.046	-44.773
	Measured	0	86.7	-126	-43
Port 4 **(set 4)**	**Theoretical**	0	90	45	135
	Simulated	0	90	45.227	135.04
	Measured	0	89	48	143

Table 1. Phases associated with the selected port of the 4×4 Butler matrix

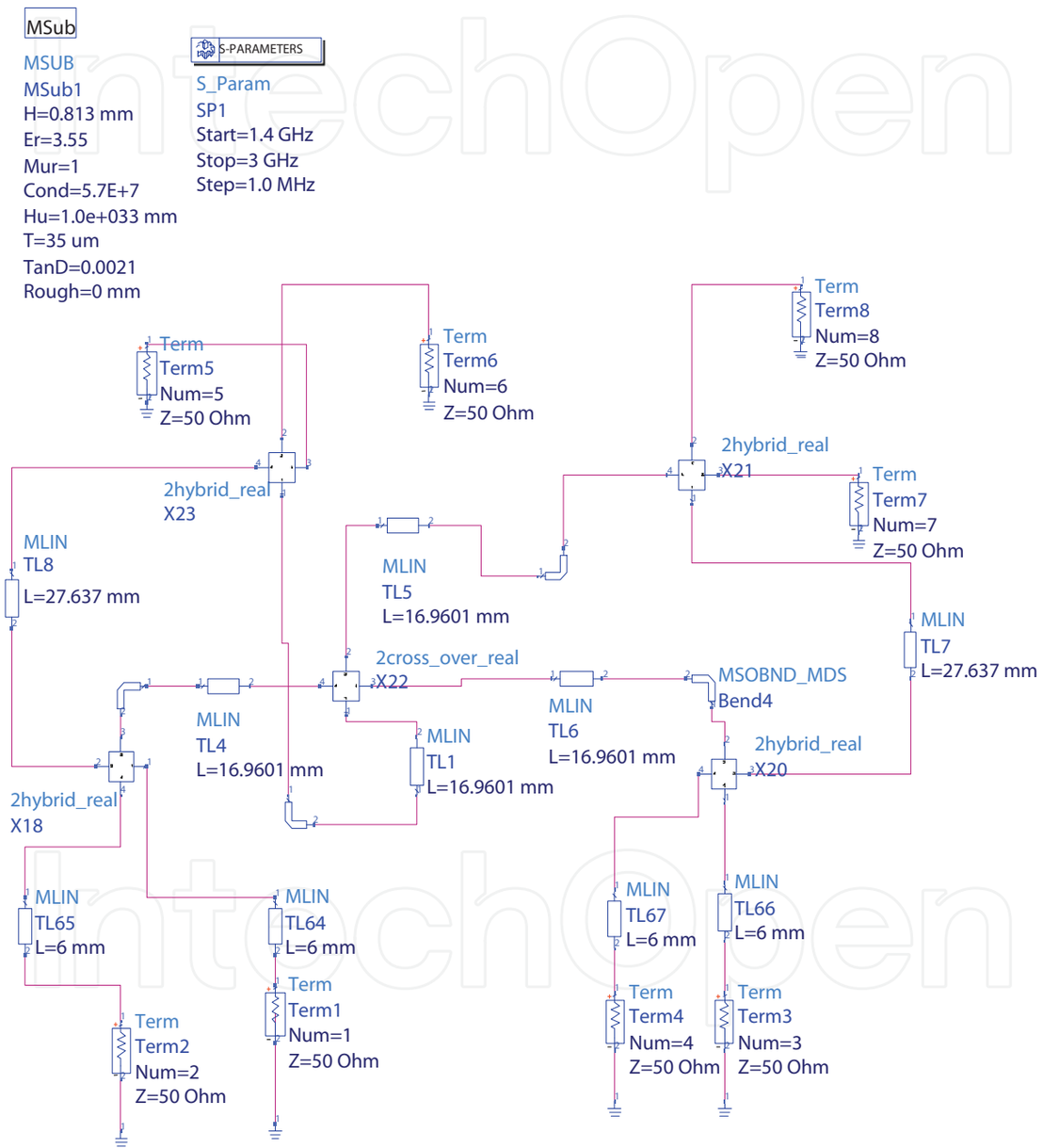


Fig. 5. ADS schematic for 4×4 Butler matrix

2.2.1 Design of quadrature hybrid

The design of a quadrature hybrid is based on the scattering matrix equation which can be obtained as follows [4]:

$$[S]_{Hybrid} = -\frac{1}{\sqrt{2}}\begin{bmatrix} 0 & j & 1 & 0 \\ j & 0 & 0 & 1 \\ 1 & 0 & 0 & j \\ 0 & 1 & j & 0 \end{bmatrix} \tag{2}$$

The design of a quadrature hybrid using ADS is started by creating ADS schematic for the quadrature hybrid using ideal transmission lines as shown in Figure 6 [3].

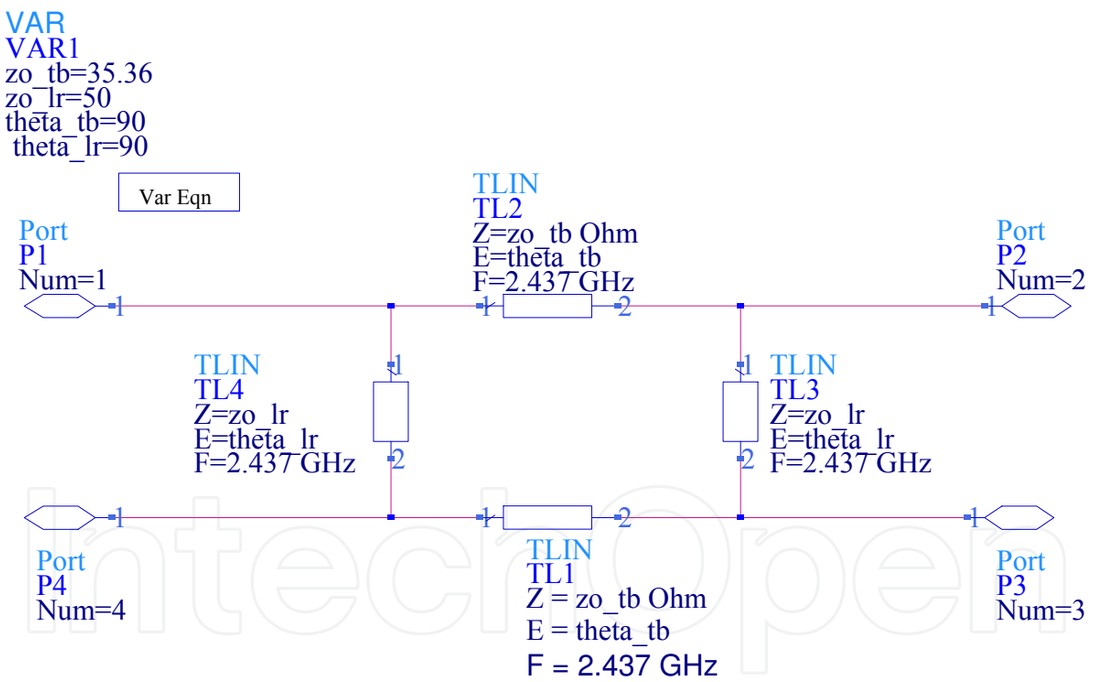


Fig. 6. ADS schematic for an ideal quadrature hybrid

Then a new ADS schematic for the quadrature hybrid is created using a microstrip substrate element (MSUB) and real transmissions lines as shown in Figure 7.
Figure 8 shows the higher level ADS schematic which is used to optimize and modify the dimensions of the real quadrature hybrid to emulate the ideal quadrature hybrid as closely as possible.
The simulated S-parameters of the real quadrature hybrid indicate that the power entering in any port is not reflected, and it is equally divided between two output ports that are existed at the other side of the hybrid, while no power is coupled to the port which is existed at the same side of the input port. This quadrature hybrid can operate over a bandwidth from 1.9 GHz to 2.8 GHz as shown in Figure 9.

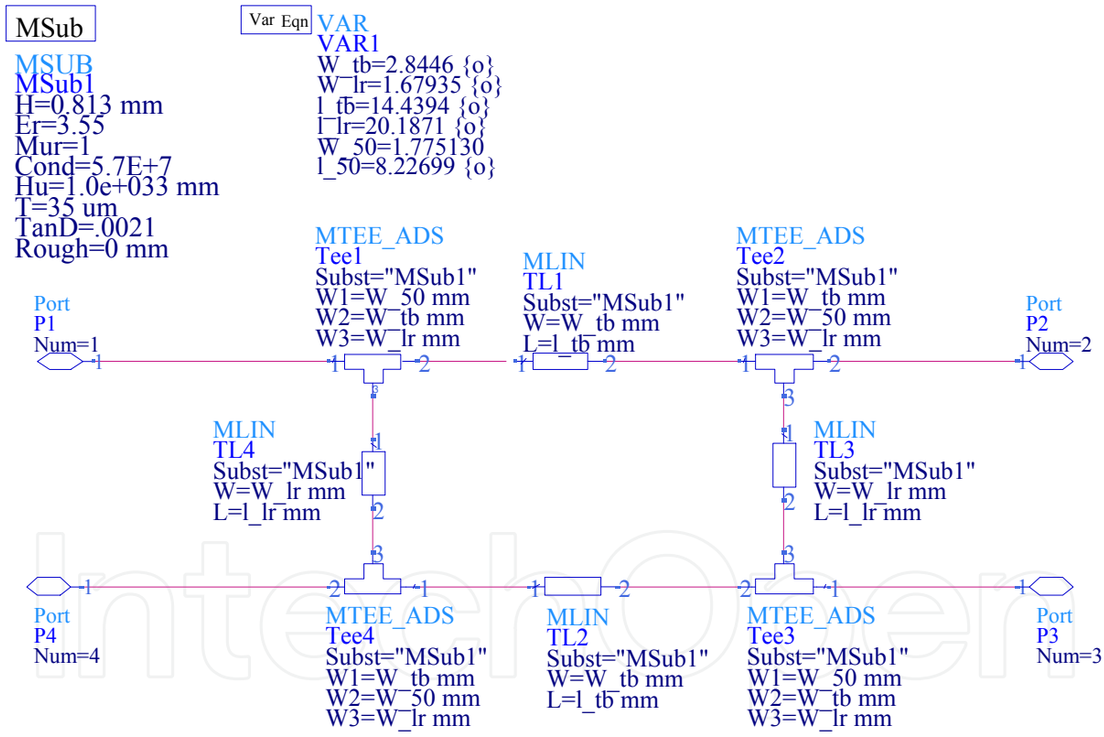


Fig. 7. ADS schematic for a real quadrature hybrid

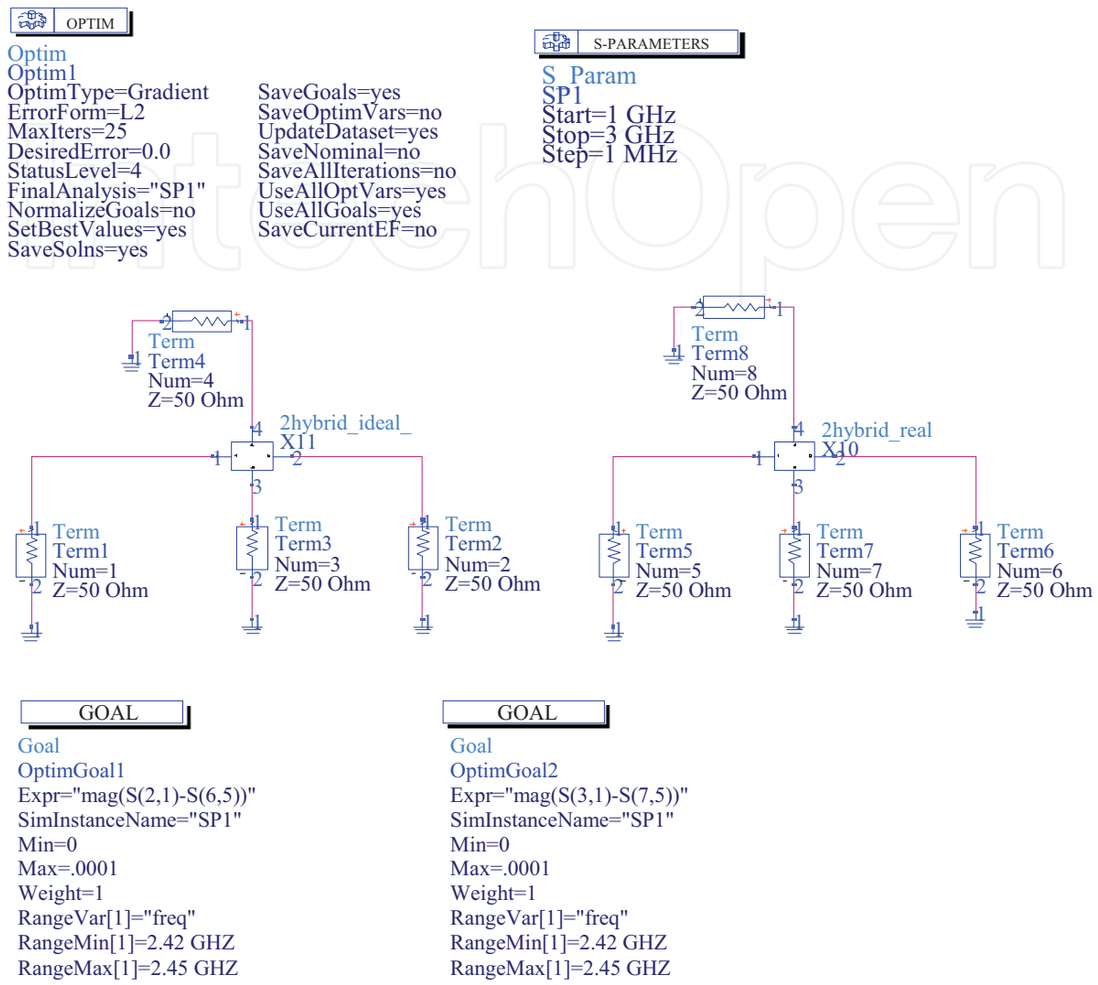


Fig. 8. Higher level ADS schematic to optimize the dimensions of the real quadrature hybrid

2.2.2 Design of crossover

The crossover provides an efficient mean to isolate two crossing transmission lines. The design of the crossover depends on the following scattering matrix equation [5].

$$[S]_{Crossover} = \begin{bmatrix} 0 & 0 & j & 0 \\ 0 & 0 & 0 & j \\ j & 0 & 0 & 0 \\ 0 & j & 0 & 0 \end{bmatrix} \tag{3}$$

A planar crossover can be designed by creating a new ADS schematic for the ideal crossover as shown in Figure 10 [3].

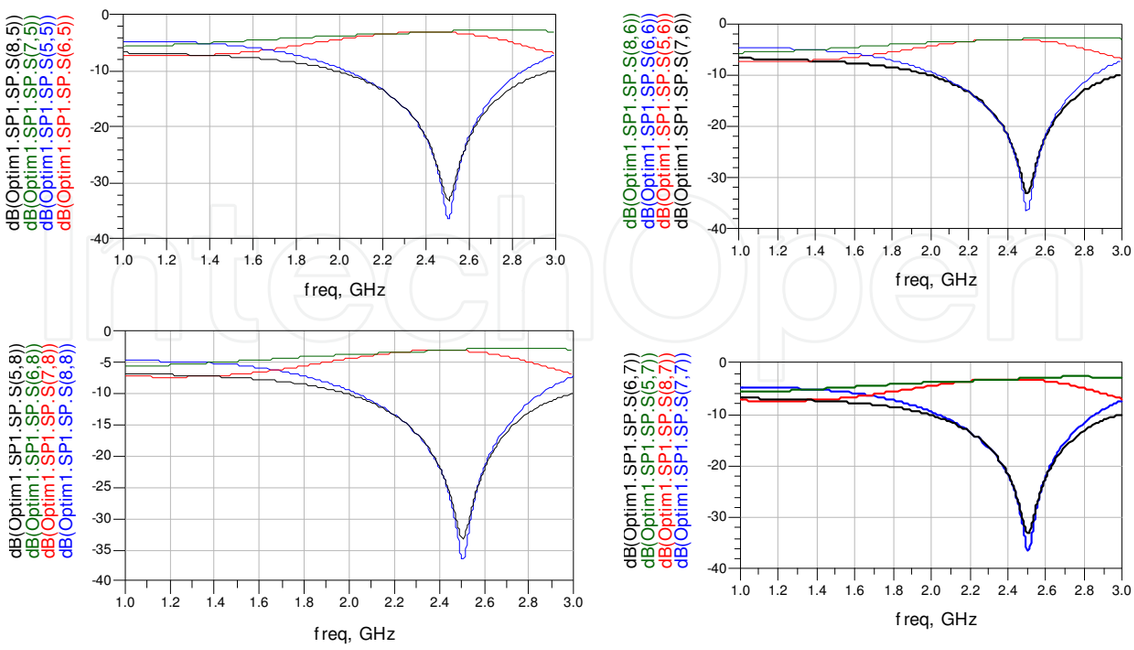


Fig. 9. Simulated S-parameters of the real quadrature hybrid

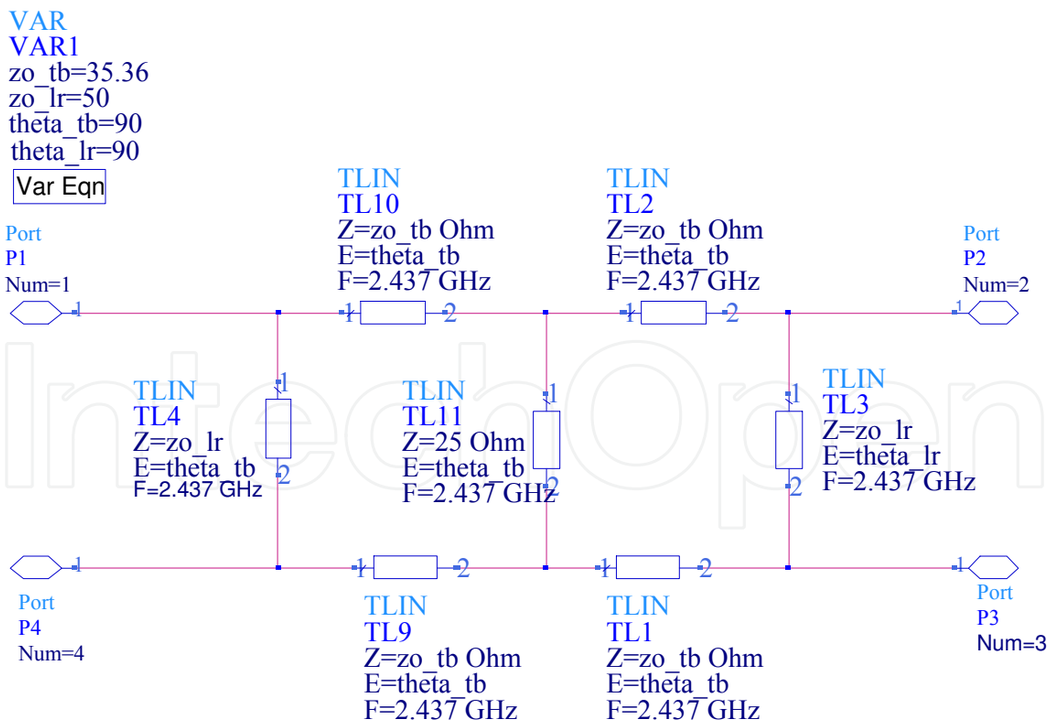


Fig. 10. ADS schematic for the ideal crossover

Figure 11 shows the ADS schematic for the real microstrip crossover.

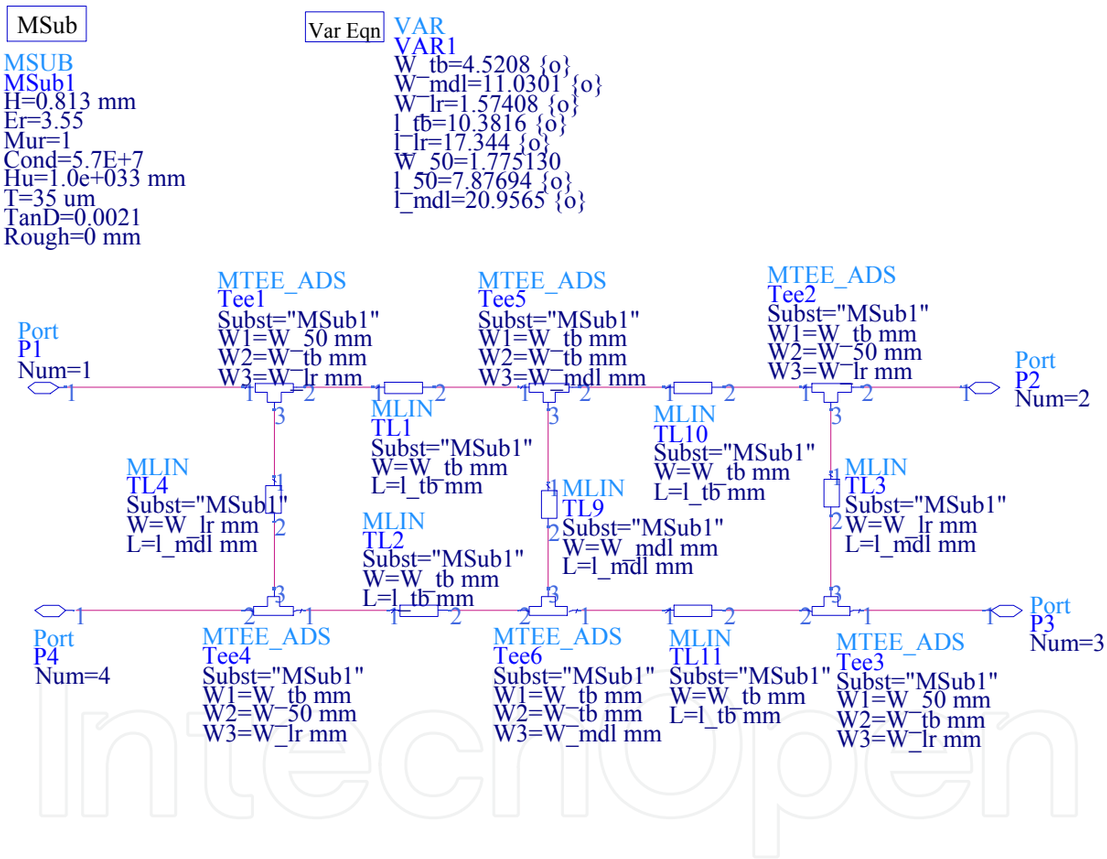


Fig. 11. ADS schematic for the real microstrip crossover

The dimensions of the real crossover are modified and optimised by using the higher level ADS schematic shown in Figure 12.

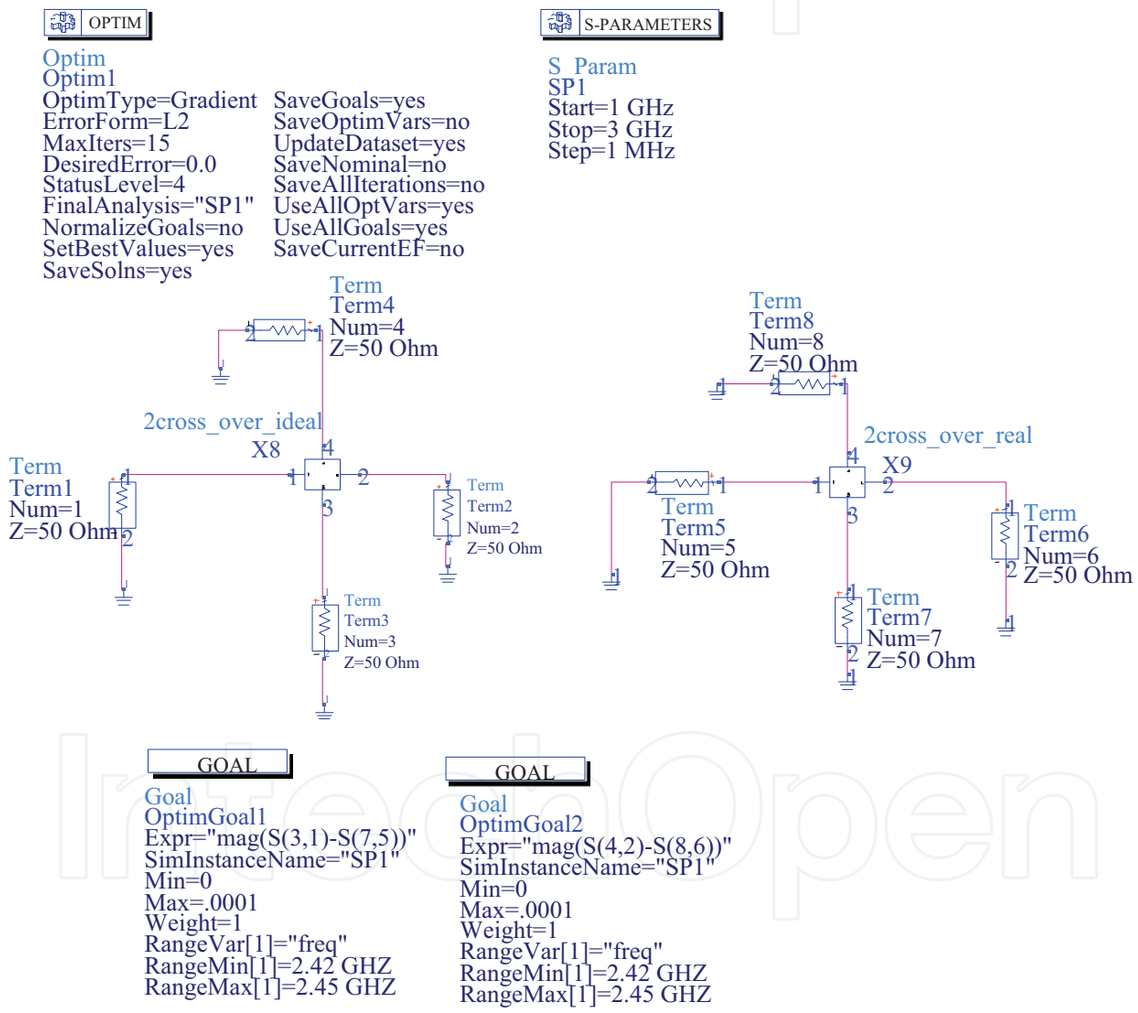


Fig. 12. Higher level ADS schematic to optimize the dimensions of the real crossover

The simulated S-parameters of the real crossover are shown in Figure 13. The bandwidth of the crossover is extended from 2 GHz to 2.8 GHz.

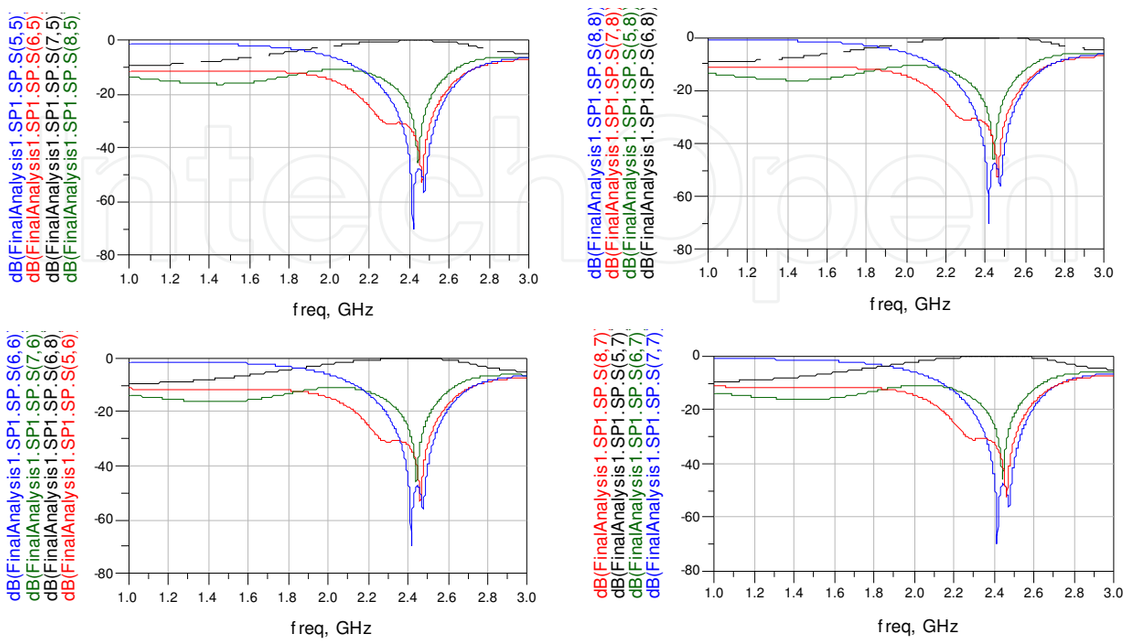


Fig. 13. Simulated S-parameters of the real crossover

2.2.3 Design of phase shifter

The phase shifter introduces a phase shift in the signal and can be implemented by adding a bit of length to a microstrip transmission line. The ADS is used to determine the length of red sections microstrip transmission lines which introduces phase shift ($\theta^{\circ}_{shift} - 45^{\circ}$) in the signal that passes through the crossover. θ°_{shift} is the phase shift of the signal passing through the black section microstrip transmission line as shown in Figure 14. θ°_{shift} is determined by finding the length of the black section, then using ADS LineCalc tool to calculate the phase shift. This phase shifter should be replaced by a Schiffman phase shifter for wideband applications [6].

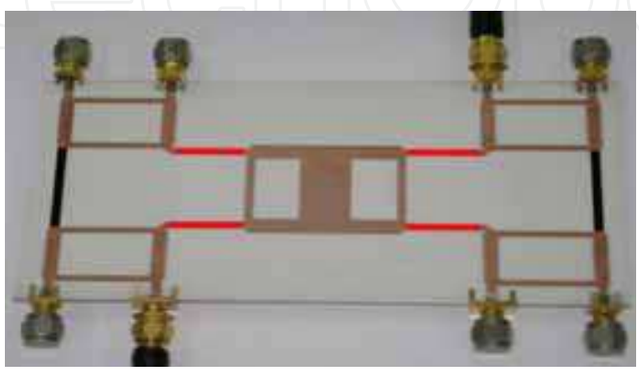


Fig. 14. Fabricated 4×4 Butler matrix

2.2.4 Design of paths between a 4×4 Butler matrix and a planar antenna array

The phases associated with each port of the 4×4 Butler matrix will be changed and the circular polarization cannot be obtained if the paths connecting the 4×4 Butler matrix with the planar antenna array do not have the same phase shift. Hence these paths are designed with the same phase shift. The path connecting antenna 1and Butler matrix is considered as the reference. The ADS is used to modify the length of the other paths to make its phases as close as possible to the phase of the reference path. Figure 15 shows the ADS schematic for path 2 which connects antenna 2 and Butler matrix. The length of this path is modified and optimized using ADS as shown in Figure 16.

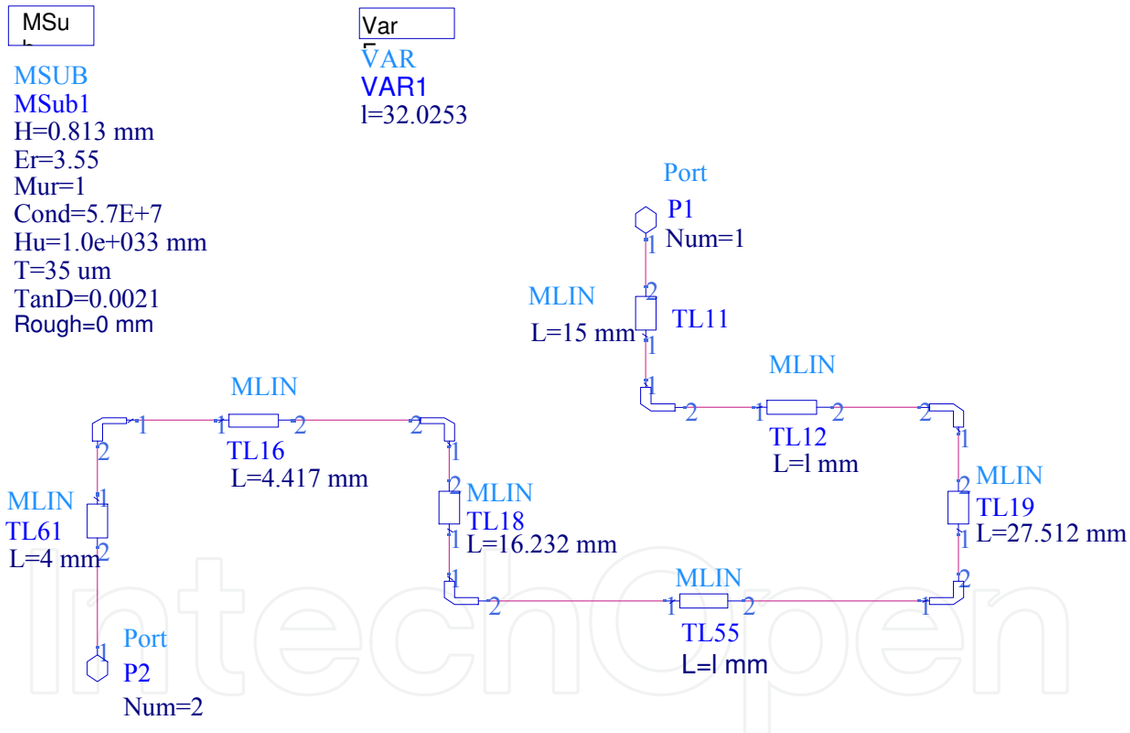


Fig. 15. ADS schematic for the path connecting antenna 2 and Butler matrix

The ADS simulated results for phases of path 2 and reference path are shown in Figure 17. The ADS schematics for designing path 3 and path 4 are given in Appendix A.

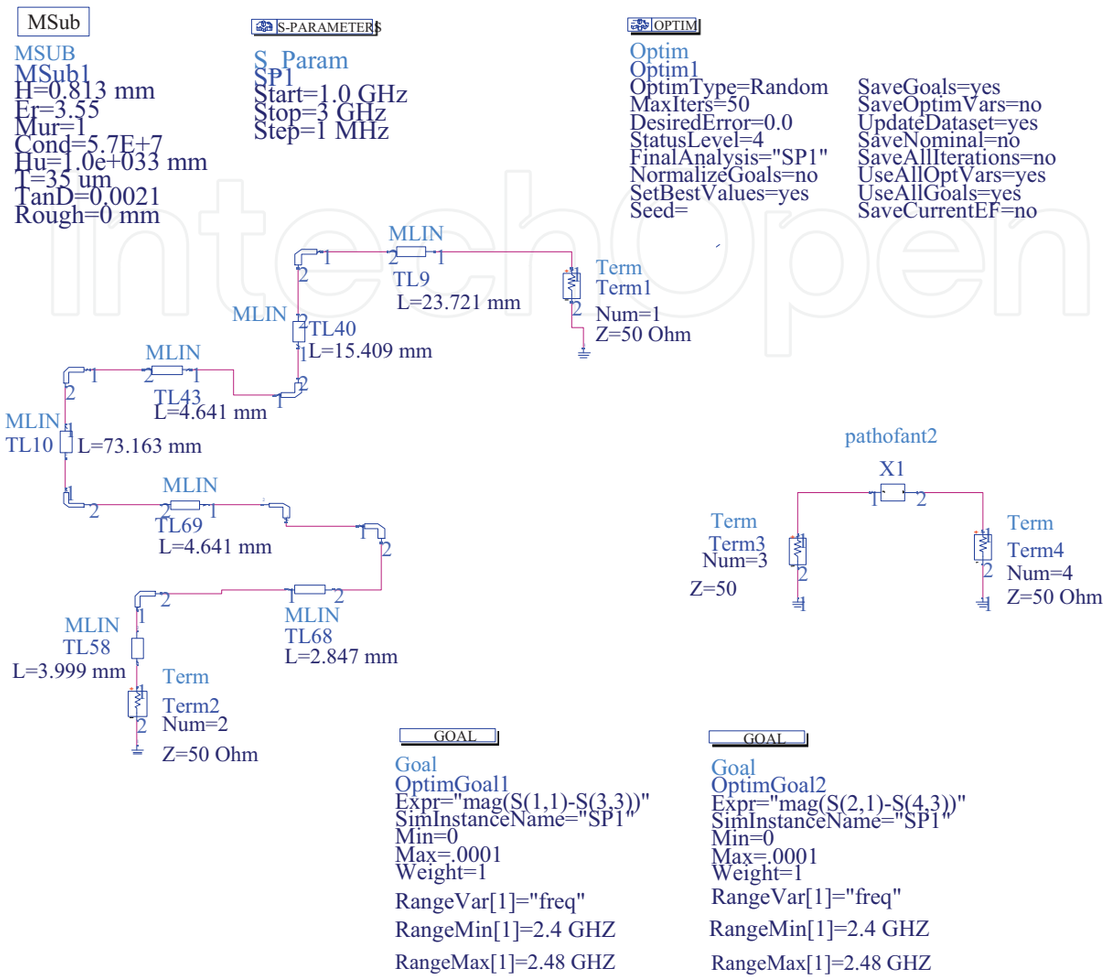


Fig. 16. ADS schematic to modify the length of path 2

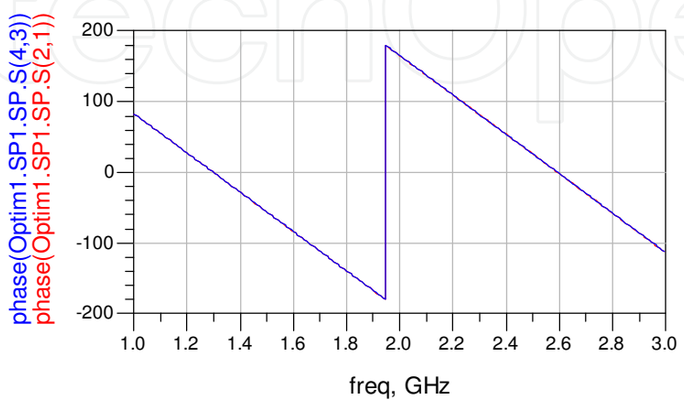


Fig. 17. ADS simulated results for phases of path 2 and reference path

2.3 Analysis of planar microstrip antenna array with Butler matrix

A planar microstrip antenna array consists of four orthogonally oriented inset-fed rectangular patch antennas as shown in Figure 18. The circular polarization can be generated with linearly polarized elements when all the adjacent elements are orthogonally oriented and are fed by a Butler matrix to form two orthogonally polarized *E*-fields from the four linearly polarized *E*-fields of the planar array elements [7,8]. The normalized instantaneous *E*-fields in *x*- and *y*-directions are represented by equations (4) and (5) respectively:

$$E_{x_planar} = \cos(\omega t - K_o z + A) + \cos(\omega t - K_o z + C) \tag{4}$$

$$E_{y_planar} = \cos(\omega t - K_o z + B) + \cos(\omega t - K_o z + D) \tag{5}$$

where K_o is the propagation constant in free space and ω is the angular frequency. The values of A, B, C and D phases in the above equations are changed according to the selected port of 4×4 Butler matrix. The instantaneous field of the plane wave traveling in positive *z*-direction is given by

$$E(z,t) = E_{x_planar}\hat{x} + E_{y_planar}\hat{y}. \tag{6}$$

For the planar microstrip antenna array that consisted of identical patches, the magnitude of E_{x_planar} is equal to E_{y_planar} .

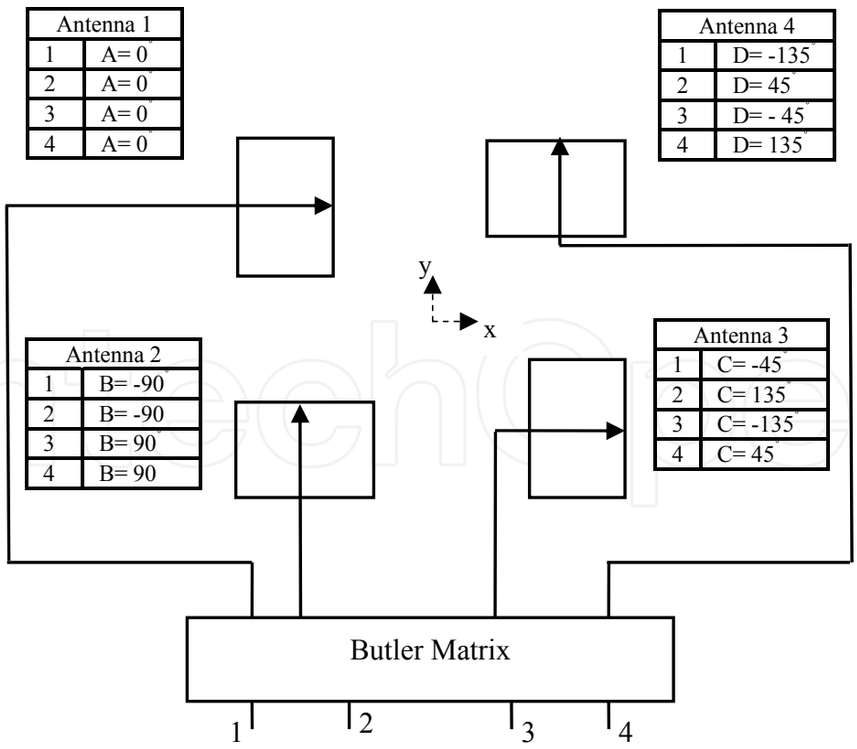


Fig. 18. Phases associated with each port of the planar microstrip antenna array with 4×4 Butler matrix

As shown in Figure 18, when port 1 or port 2 is selected, the phase delay between E_{y_planar} and E_{x_planar} will be $-\frac{\pi}{2}$ and RHCP is generated. The LHCP is obtained when port 3 or port 4 is selected because the phase delay between E_{y_planar} and E_{x_planar} will be $+\frac{\pi}{2}$.

2.4 Radiation pattern for planar microstrip antenna array

The total normalized *E*-plane radiation pattern of the planar microstrip array is obtained by the following equation [9]:

$$E_{T_\theta} = E_{\theta} \left| AF_{T_E} \right| . \tag{7}$$

where $\left| AF_{T_E} \right|$ is the normalized *E*-plane array factor for the planar microstrip array and can be obtained from equation (8) [10]:

$$\left| AF_{T_E} \right| = \left(1 + e^{j(K_o d_x \sin\theta + \phi_x)}\right) \left(1 + e^{j\phi_y}\right) \tag{8}$$

E_{θ} is the total normalized *E*-plane radiation pattern of a single microstrip patch antenna and is obtained by equation (9) [11]:

$$E_{\theta} = \left| 1 + e^{jK_o L \sin\theta} \right| \tag{9}$$

where θ is the elevation angle and L is the length of the microstrip patch antenna. The total normalized radiation pattern and the normalized array factor for the *H*-plane are obtained from equations (10) and (11) respectively [9]:

$$H_{T_\theta} = H_{\theta} \left| AF_{T_H} \right| \tag{10}$$

$$\left| AF_{T_H} \right| = \left(1 + e^{j(K_o d_y \sin\theta + \phi_y)}\right) \left(1 + e^{j\phi_x}\right) \tag{11}$$

where ϕ_x, ϕ_y are the feeding phases for the antenna 4 and the antenna 2 respectively. d_x, d_y are the spacings between patches in the *x*-direction and *y*-direction respectively. equation (12) is used to determine the total normalized *H*-plane radiation pattern of a single microstrip patch antenna (H_{θ}) [11];

$$H_{\theta} = \frac{\sin(\frac{K_o W}{2}\sin\theta)}{\frac{K_o W}{2}\sin\theta} \cos\theta \ . \tag{12}$$

where *W* is the width of the microstrip patch antenna.

2.5 Simulation and measured results

To design the planar microstrip antenna array, the spacing distance between the patches in *x*-direction (d_x) is determined based on the simulation of equations (7), (8) and (9) using

Matlab. Figure 19 shows the total normalized *E*-plane radiation pattern of the planar microstrip array (E_{T_θ}) versus the elevation angle θ at different values of d_x.

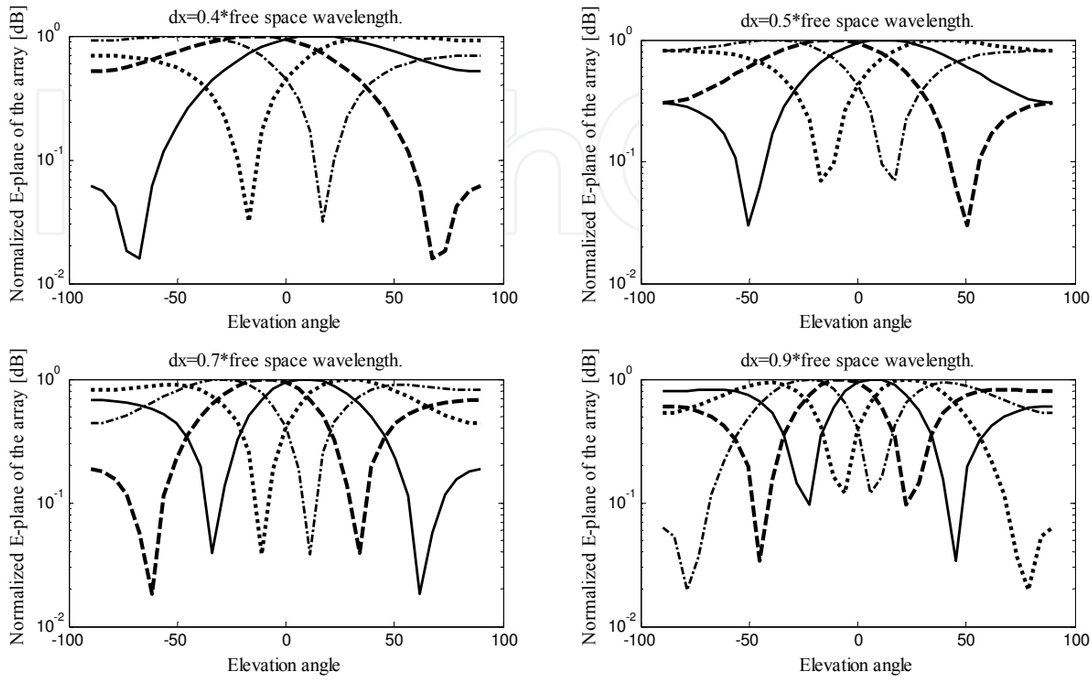


Fig. 19. Simulated normalized *E*-plane radiation pattern of the planar microstrip antenna array versus an elevation angle (— feed at port 1, −· feed at port 2, … feed at port 3, --- feed at port 4)

The fixed beams get narrowed as d_x is increased, but to maintain balance between the narrowed beams and small-size antenna array, and also to avoid the grating lobes, d_x=0.5*(free space wavelength) is selected. d_y is determined based on the simulation of equations (10), (11) and (12) using Matlab. The total normalized *H*-plane radiation pattern (H_{T_θ}) versus the elevation angle θ is shown in Figure 20.

The value of H_{T_θ} is equal to the value of E_{T_θ} divided by the intrinsic impedance of the free space; so H_{T_θ} is not sensitive to the change in the separation distance d_y because its value is much smaller than that of E_{T_θ}. However, d_y=0.5*(free space wavelength) is selected to maintain a balance between the avoidance of mutual coupling and the small-size antenna array. The set of curves in Figures 19 and 20 represents the normalized *E*-plane and *H*-plane respectively; each curve is generated by selecting a different feed port of the 4×4 Butler matrix.

The planar microstrip antenna array with 4×4 Butler matrix is fabricated using Rogers's substrate of thickness h_t=0.85 mm, loss tangent=0.0021 and dielectric constant $\varepsilon_r = 3.55$. The inset-fed rectangular microstrip patch antenna is designed at a resonant frequency equal to 2.437 GHz using Matlab and then simulated using ADS [12]. The parameters for the substrate layers and metallization layers of the Rogers's substrate are created in the ADS Momentum as shown in Figures 21 and 22 respectively.

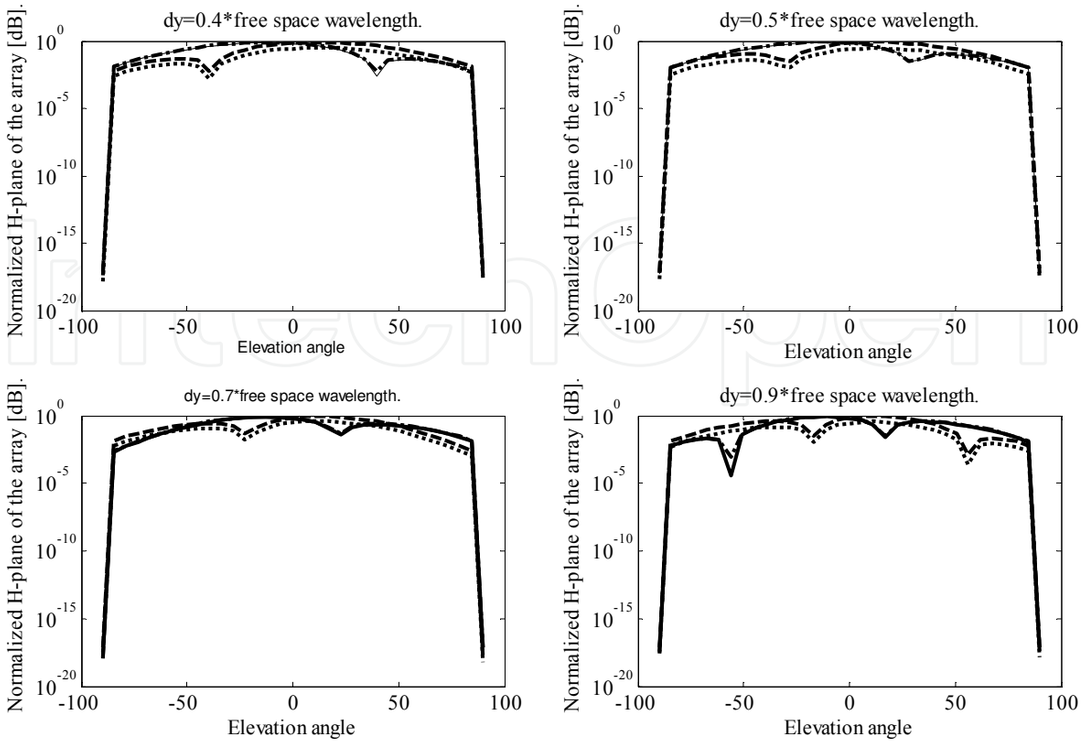


Fig. 20. Simulated normalized *H*-plane radiation pattern of the planar microstrip antenna array versus an elevation angle (— feed at port 1, −· feed at port 2, … feed at port 3, --- feed at port 4)

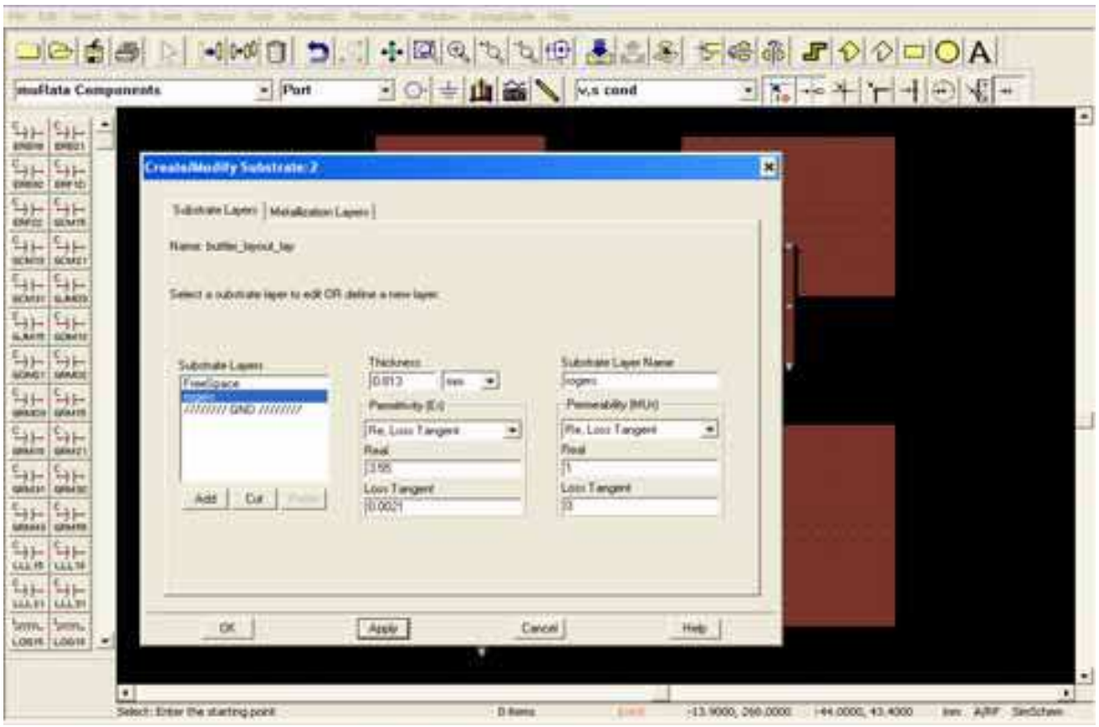


Fig. 21. Parameters setup in ADS Momentum for substrate layers of the Rogers's substrate

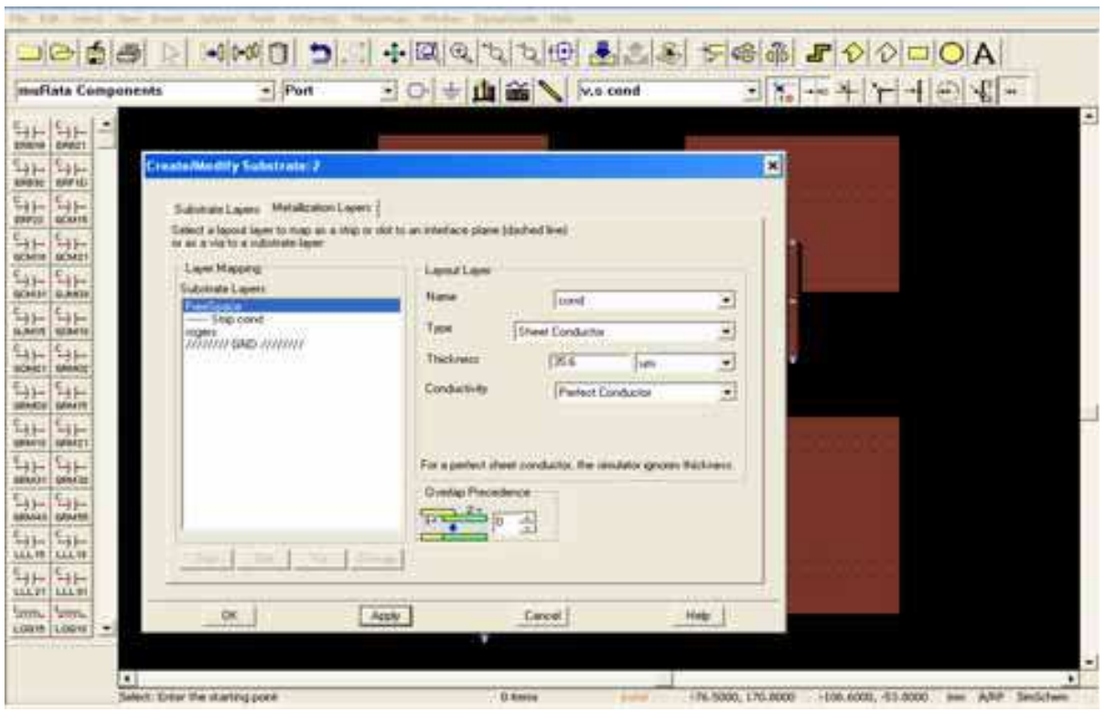


Fig. 22. Parameters setup in ADS Momentum for metallization layers of the Rogers's substrate

Figure 23 shows the ADS Momentum for the planar microstrip antenna array.

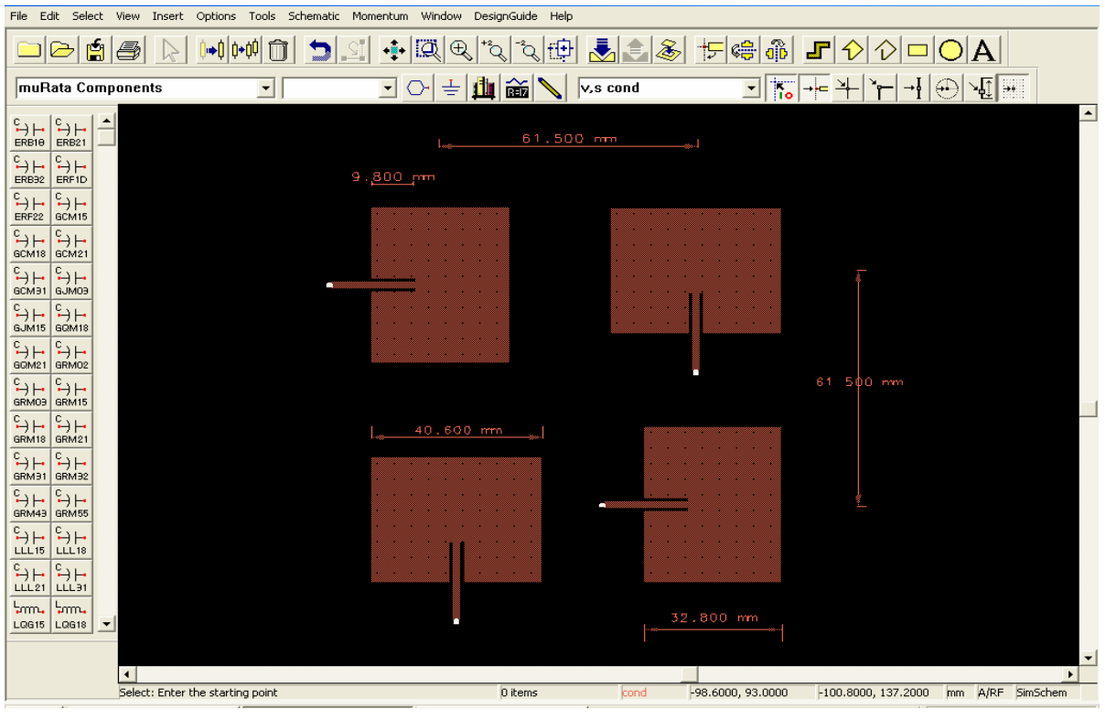


Fig. 23. ADS Momentum for the planar microstrip antenna array

The planar array is simulated by using ADS Momentum and then the Momentum dataset file is imported to the ADS schematic to simulate the planar microstrip antenna with Butler matrix as shown in Figure 24.

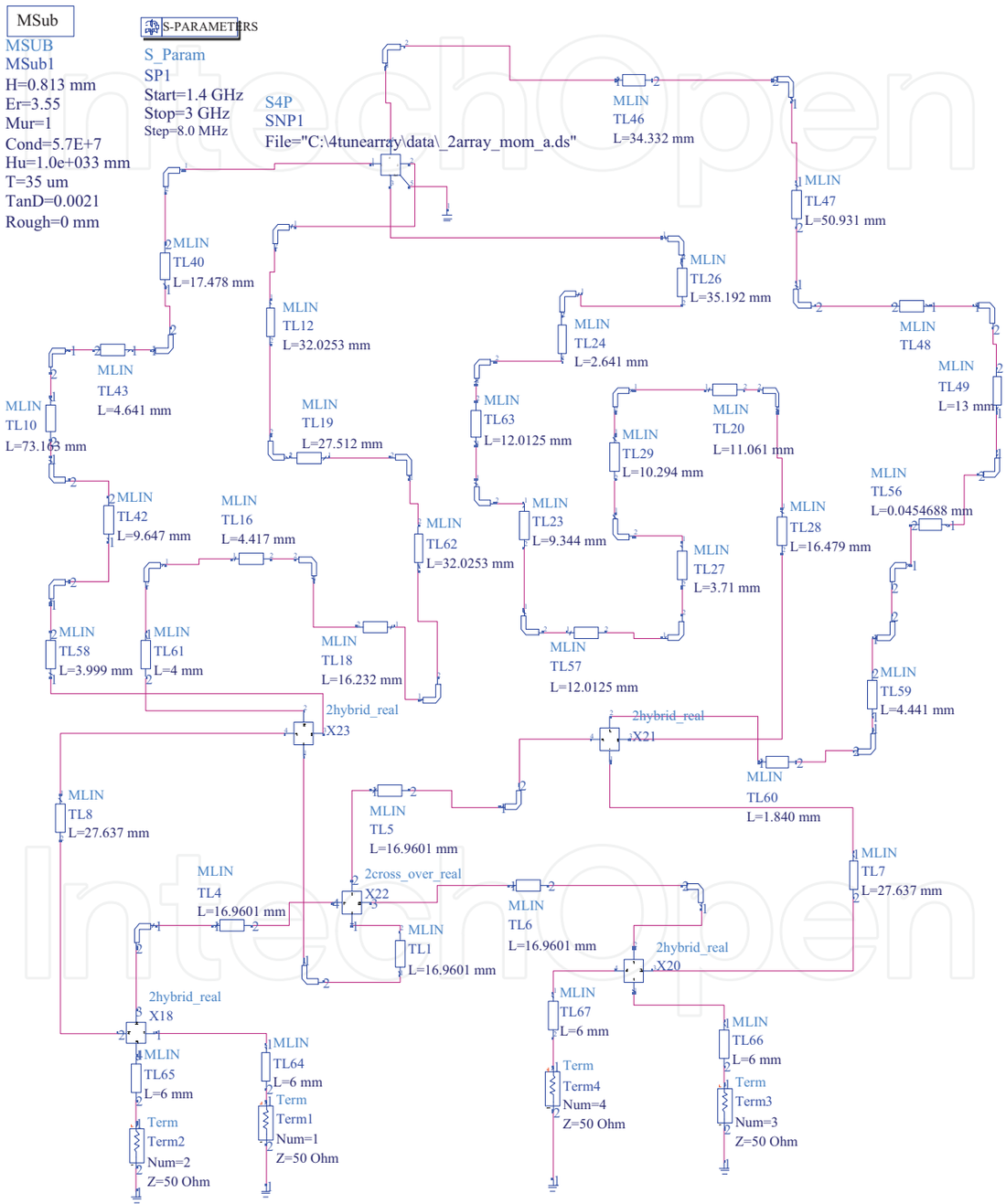


Fig. 24. ADS schematic diagram for simulating the planar microstrip antenna with 4×4 Butler matrix

Figure 25 shows the ADS layout of the planar mirostrip antenna array with 4×4 Butler matrix. The Fabricated planar microstrip antenna array with 4×4 Butler matrix is shown in Figure 26.

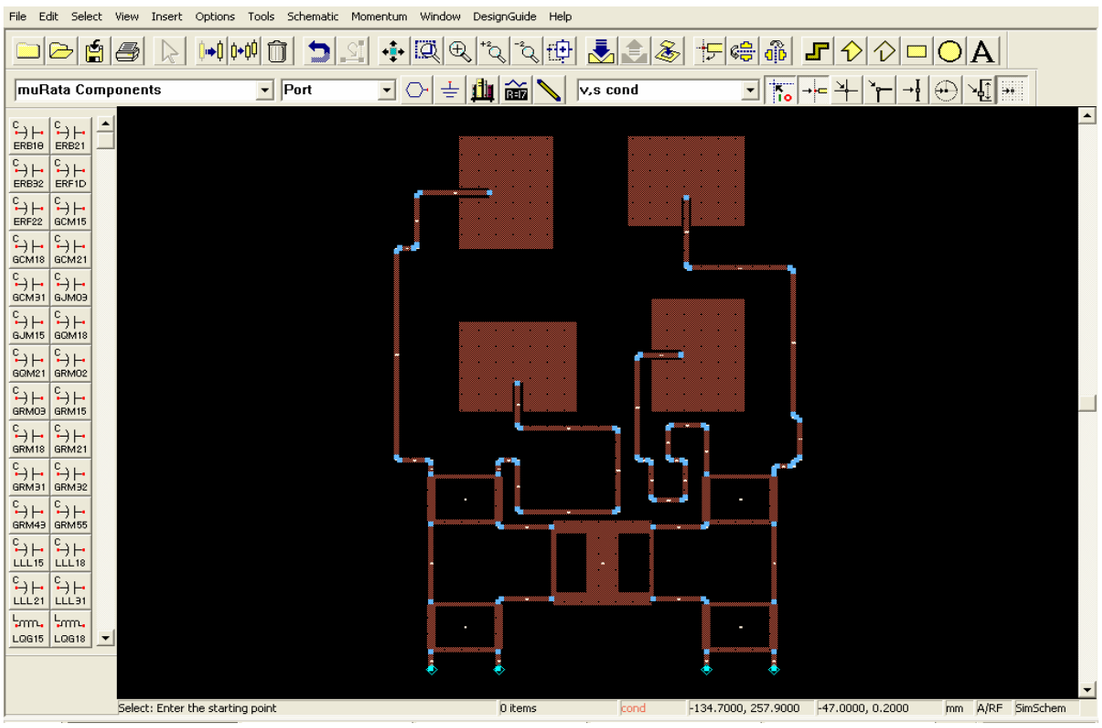


Fig. 25. ADS layout of the planar microstrip antenna array with 4×4 Butler matrix

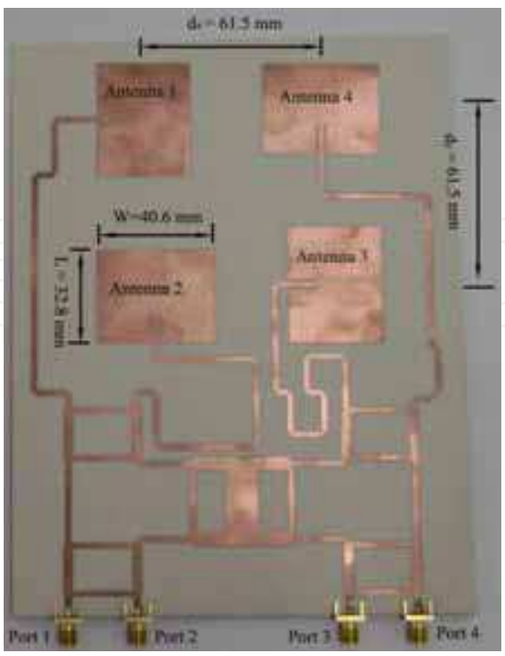


Fig. 26. Fabricated planar microstrip antenna array with 4×4 Butler matrix

The measured and the simulated values of the reflection coefficient at each port of the planar microstrip antenna array with 4×4 Butler matrix versus the frequency band of 1.4–3 GHz are shown in Figure 27.

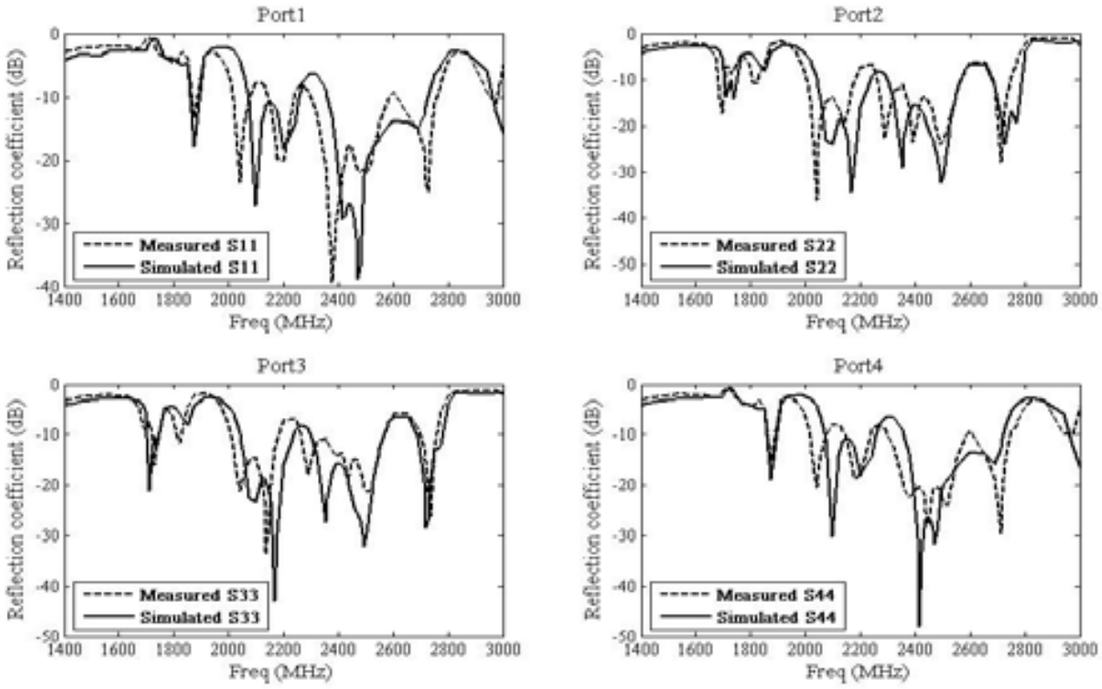


Fig. 27. Reflection coefficients versus frequency for the planar microstrip antenna array with 4×4 Butler matrix

The phases associated with the ports of the Butler matrix result in the existence of different voltages and different input impedances at the ports of the Butler matrix. Hence the reflection coefficients at these ports will not be the same owing to the relationship between the reflection coefficient and input impedance. The mutual coupling between the patches induces frequency modes. These modes are matched with 50 Ω impedance outside the required 2.437 GHz range (i.e. for port 1, the measured reflection coefficient is less than −10 dB at ranges 1864–1885 MHz, 2014–2073 MHz, and 2145–2237 MHz owing to the effect of mutual coupling between the patches). The mutual coupling impedances between the patches are different because of the effect of the phases associated with the ports of the Butler matrix. Due to the dissimilarity of the mutual coupling impedances, each port will have reflection coefficient less than −10 dB over different frequency ranges outside the required bandwidth [13]. Although the Butler matrix reflection coefficients are not the same at all the ports, they have good values over the required bandwidth. The measured impedance bandwidth (for reflection coefficient < −10 dB) at port 1, port 2, port 3, and port 4 are 18.8%, 12.52%, 12.5%, and 18.5 %, respectively. The obtained impedance bandwidth of this planar array is high when compared with a single microstrip patch antenna that achieves 0.7% impedance bandwidth as shown in Figure 28 [14]. The implementation of the Butler matrix gives a wide band due to the absorption of the reflected power in the matched loads connected to the non-selected ports of the butler matrix. Moreover, the mutual coupling between the patches enhances the bandwidth [13].

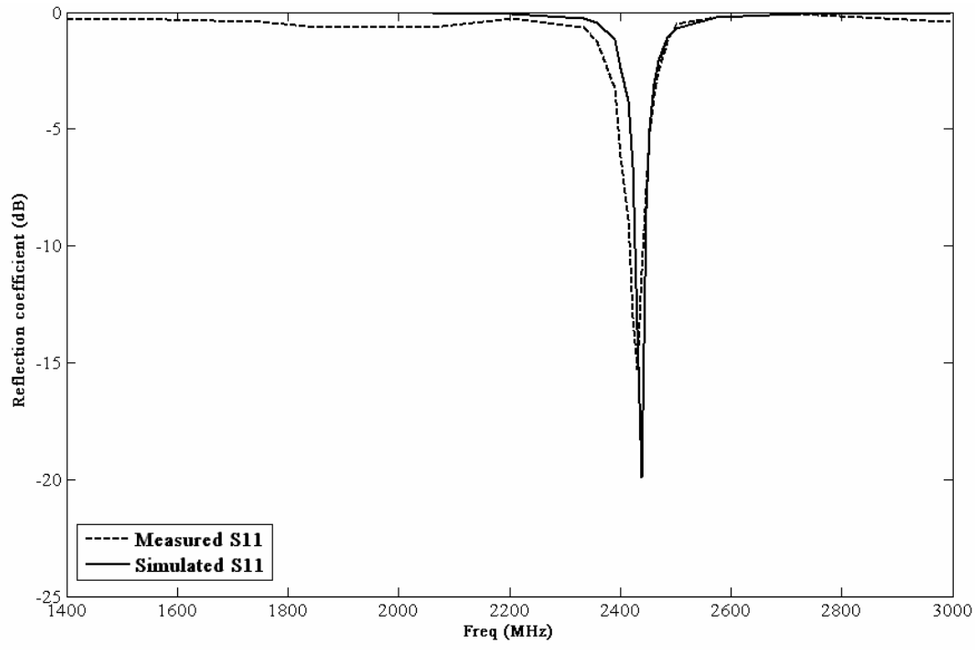


Fig. 28. Reflection coefficient versus frequency for an inset-fed rectangular microstrip patch antenna

The measured normalized radiation pattern of the planar microstrip antenna array with 4×4 Butler matrix is shown in Figure 29. The planar microstrip antenna array that is fed by the 4×4 Butler matrix has four beams at four different directions. These beams have a circular polarization diversity because a beam with RHCP will be obtained when port 1 or 2 is selected, but if port 3 or 4 is selected a beam with LHCP will be generated. The measured gains at 2.437 GHz for ports 1, 2, 3 and 4 are 9.74 dBi, 8.6 dBi, 9 dBi and 10.1 dBi respectively. The gain of port 1 and port 2 is measured using right hand circularly polarized standard antenna (2.4 GHz, 8 dBi, RHCP, Flat Patch Antenna), while the gain for port 3 and port 4 is measured using left hand circularly polarized standard antenna (2.4 GHz, 8dBi, LHCP, Flat Patch Antenna).

The measured axial ratios of the individual ports versus the elevation angle are shown in Figure 30. A good axial ratio (axial ratio < 3 dB) of ports 1, 2, 3 and 4 are achieved over angular ranges −36° to 61°, −55° to −9°, −31° to 81° and −90° to 15°respectively.

Radiation pattern and axial ratio measurements are carried out in a near field Satimo chamber as shown in Figure 31. The measurement system consists of probe antennas mounted with equal spacing on a circular arch. The measurements of the radiation pattern and the axial ratio can be obtained by electronic switching of the probe antennas. The measured data is collected automatically and saved in MS Excel format.

The impedance bandwidth of the planar array with Butler matrix can be extended by using a thicker substrate. The obtained impedance bandwidth is 37% for ports 1 and 4, while ports 2 and 3 have an impedance bandwidth equal to 20% as shown in Figure 32. This is when using FR4 substrate (h_t=1.6 mm, loss tangent=0.035, and dielectric constant $\varepsilon_r = 5.4$). But the FR4 substrate has a poor loss tangent which results in lower efficiency and therefore the gain will be decreased [15].

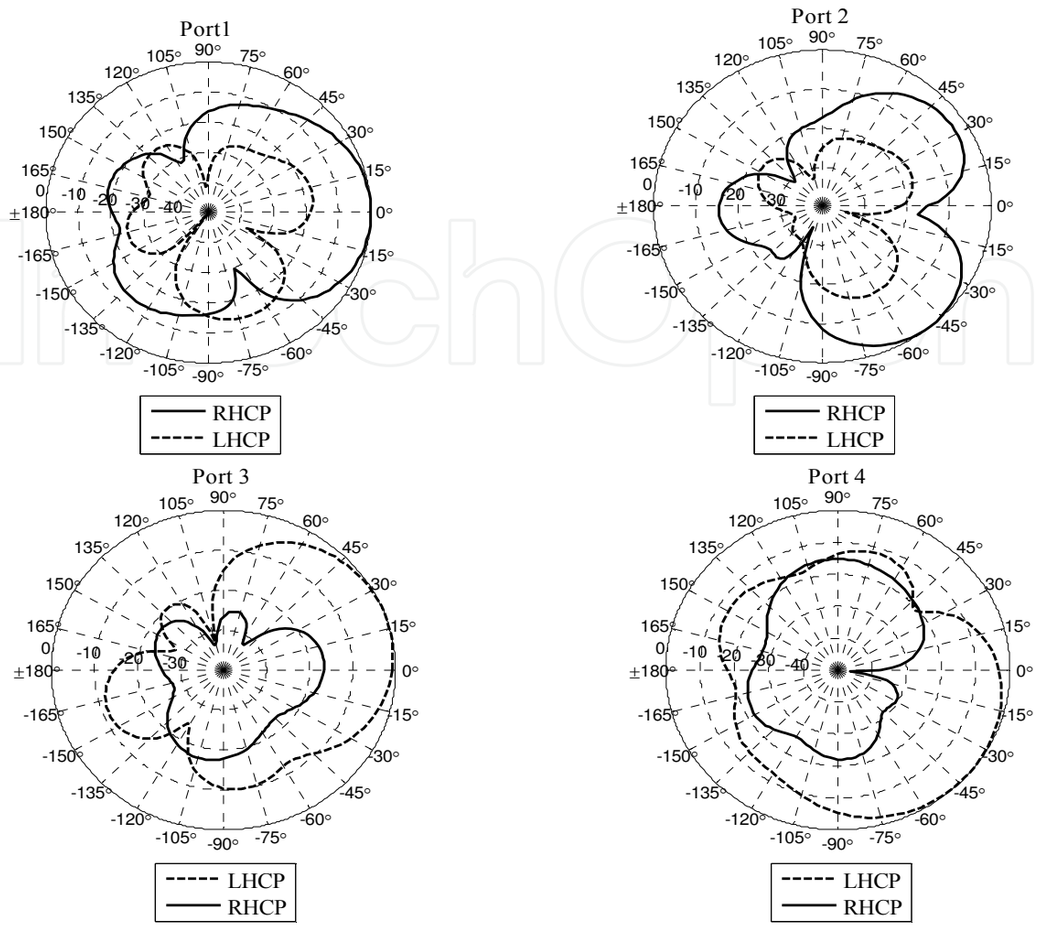


Fig. 29. Measured normalized radiation pattern of the planar microstrip antenna array with 4×4 Butler matrix at 2.437 GHz

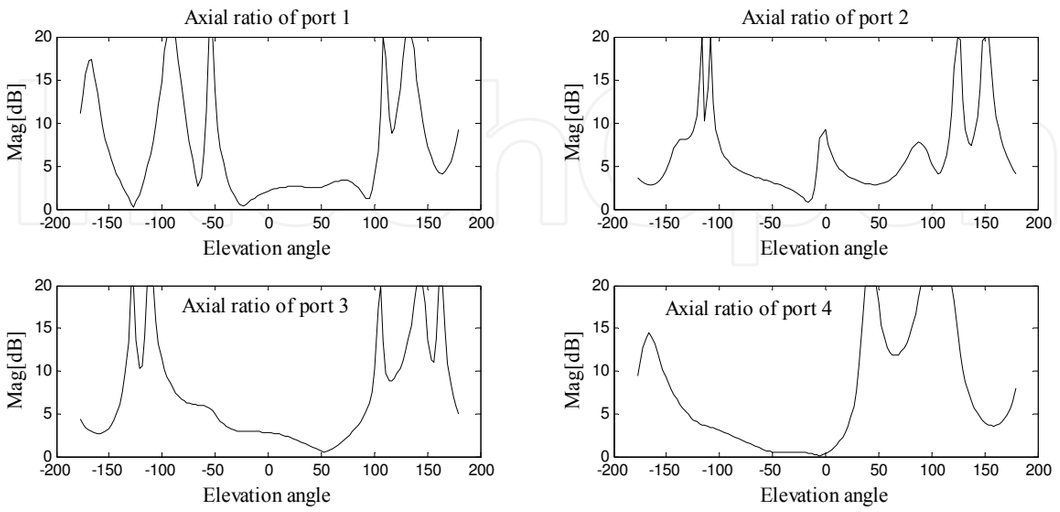


Fig. 30. Measured axial ratios of the planar microstrip antenna array with 4×4 Butler matrix at 2.437 GHz

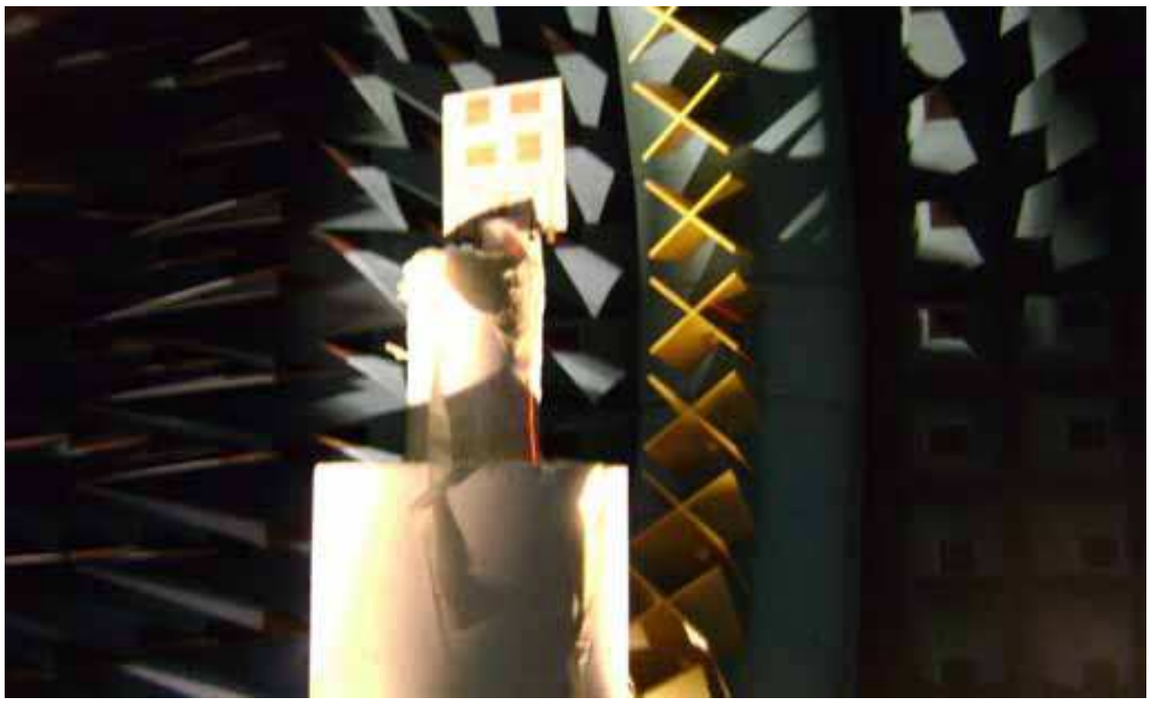


Fig. 31. Measuring a planar microstrip antenna with Butler matrix inside near field Satimo chamber

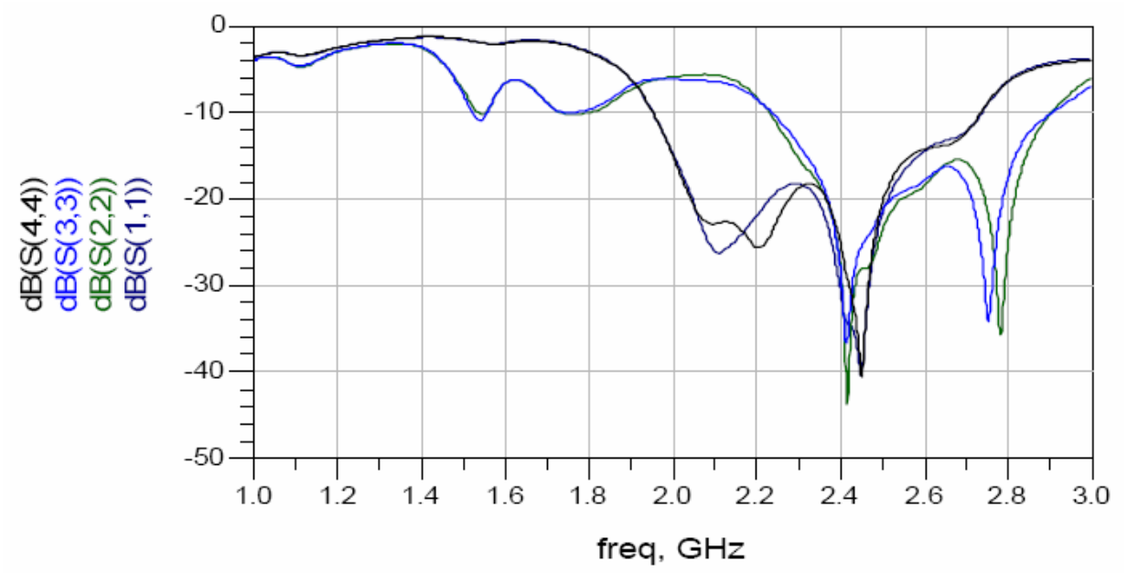


Fig. 32. Simulated reflection coefficients versus frequency for the planar microstrip antenna array with 4×4 Butler matrix using FR4 substrate

3. Analysis, design, and implementation of an aperture-coupled microstrip antenna

The circular polarization diversity with the square patch microstrip antenna is obtained by the implantation of the quadrature hybrid as a microstrip feed line. The small size antenna is achieved by using the aperture coupled structure. In the present study, the ACMSA is analyzed based on cavity model because the TLM is useful only for patches of rectangular shape [14]. The cavity model is used to design the ACMSA and determine the length of the open microstrip stub line in order to match microstrip antenna. The Matlab and ADS are used for designing and simulating the ACMSA.

3.1 Analysis of ACMSA using cavity model

3.1.1 Resonant Frequency

The cavity model is based on treating the microstrip antennas as cavities formed by microstrip lines as shown in Figure 33. The region between the patch and ground plane may be treated as a cavity bounded by electric walls above and below, and magnetic walls along the edges. The fields inside the antenna are assumed to be the fields inside this cavity. Due to the electrically thin substrate the fields in the interior region do not vary with z. Also inside the cavity the electric field has only a z component (E_z) and the magnetic field has H_x and H_y components [14]. Figure 33 shows the cavity model of the ACMSA.

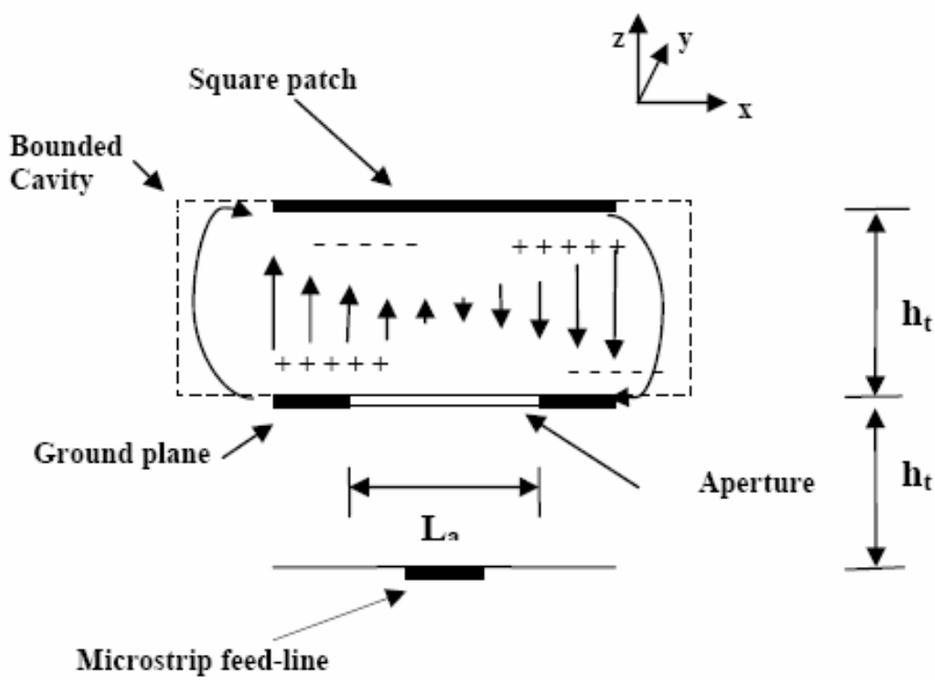


Fig. 33. Cavity model of the ACMSA

The magnetic field H inside the cavity volume can be developed by Maxwell's equations [16]:

$$\nabla \times H = J_e + j\omega\varepsilon_o\varepsilon_r E \tag{13}$$

$$\nabla \times H = \begin{vmatrix} \hat{x} & \hat{y} & \hat{z} \\ \frac{\partial}{\partial x} & \frac{\partial}{\partial y} & \frac{\partial}{\partial z} \\ H_x & H_y & 0 \end{vmatrix} \tag{14}$$

$$\nabla \times H = \left(\frac{\partial H_y}{\partial x} - \frac{\partial H_x}{\partial y} \right) \hat{z} \tag{15}$$

$$\nabla \times (\nabla \times H) = \begin{vmatrix} \hat{x} & \hat{y} & \hat{z} \\ \frac{\partial}{\partial x} & \frac{\partial}{\partial y} & \frac{\partial}{\partial z} \\ 0 & 0 & \left(\frac{\partial H_y}{\partial x} - \frac{\partial H_x}{\partial y} \right) \end{vmatrix} \tag{16}$$

$$\nabla \times (\nabla \times H) = \left(\frac{\partial^2 H_y}{\partial x \partial y} - \frac{\partial^2 H_x}{\partial y^2} \right) \hat{x} + \left(\frac{\partial^2 H_x}{\partial x \partial y} - \frac{\partial^2 H_y}{\partial x^2} \right) \hat{y} \tag{17}$$

$$\nabla \times \left(J_e + j\omega \varepsilon_o \varepsilon_r E \right) = \left(j\omega \varepsilon J_{mx} + \omega^2 \mu \varepsilon H_x \right) \hat{x} + \left(j\omega \varepsilon J_{my} + \omega^2 \mu \varepsilon H_y \right) \hat{y} \tag{18}$$

$$K = \omega \sqrt{\mu \varepsilon} \tag{19}$$

where K is the propagation constant inside the cavity, $\varepsilon = \varepsilon_o \varepsilon_r$. Equations (20) and (21) are obtained by substituting the right hand side of equation (17) into the left hand side of equation (18);

$$\frac{\partial^2 H_y}{\partial x \partial y} - \frac{\partial^2 H_x}{\partial y^2} - K^2 H_x = j\omega \varepsilon J_{mx} \tag{20}$$

$$\frac{\partial^2 H_x}{\partial x \partial y} - \frac{\partial^2 H_y}{\partial x^2} - K^2 H_y = j\omega \varepsilon J_{my} \tag{21}$$

In order to solve equation (20), the cavity model assumes that the tangential magnetic field is zero, so that J_{mx} equals to zero.

$$\frac{\partial^2 H_y}{\partial x \partial y} - \frac{\partial^2 H_x}{\partial y^2} - K^2 H_x = 0 \tag{22}$$

Letting the Eigen functions of the homogeneous wave equation (22) be Ψ_{mn} and K_{mn} be the eigenvalues of K, K_{mn} can be obtained from equation (23) as indicated in Appendix B.

$$K_{mn}^2 = K_m^2 + K_n^2 \tag{23}$$

The resonance frequency of (*m, n*) mode can be obtained by equation (24);

$$f_{mn} = \frac{cK_{mn}}{2\pi\sqrt{\varepsilon_r}} \tag{24}$$

where *c* is the speed of light, ε_r is the relative dielectric constant.

3.1.2 Magnetic field component in x-direction

The solutions of equation (20) can be expressed in the following eigenfunction expansion form [16];

$$H_x = \sum_{mn} \beta_{x,mn} \psi_{x,mn} \tag{25}$$

where $\beta_{x,mn}$ is the modes coefficients and given by (see Appendix C)

$$\beta_{x,mn} = \frac{j\omega\varepsilon}{(K_{mn}^2 - K^2)K_n^2} \int_0^{W_a} \int_0^{L_a} J_{mx} \cdot \psi_{x,mn}^* dxdy \tag{26}$$

The propagation constant (*K*) in equation (26) is replaced by the effective propagation constant (K_{eff}) because the losses of the cavity are included [2,17].

$$K_{eff}^2 = \omega^2 \mu\varepsilon_o(\varepsilon_r(1 - \frac{j}{Q})) \tag{27}$$

where *Q* is the quality factor. It is assumed that the electric field distribution in the aperture paralleled to *x* axis (E_{ay}) is in the form of a single piece-wise sinusoidal mode [18]. The distance from the square patch edge to the center of the aperture is defined as X_1 and from the square patch edge to the center of the aperture as Y_1 as shown in Figure 34.

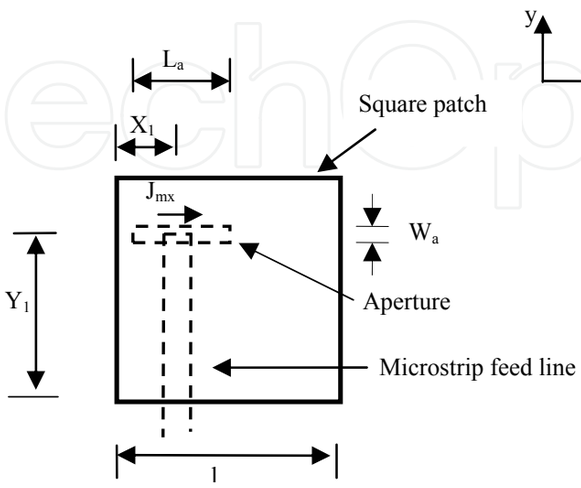


Fig. 34. Position of the aperture paralleled to *x*-axis

$$E_{\alpha y} = \frac{V_{\alpha x}}{W_a} \frac{\sin\left[K_a\left(\frac{L_a}{2} - (X_1 - x)\right)\right]}{\sin\left(K_a \frac{L_a}{2}\right)} \qquad X_1 - \frac{L_a}{2} \le x \le X_1 \tag{28}$$

$$E_{\alpha y} = \frac{V_{\alpha x}}{W_a} \frac{\sin\left[K_a\left(\frac{L_a}{2} - (x - X_1)\right)\right]}{\sin\left(K_a \frac{L_a}{2}\right)} \qquad X_1 \le x \le X_1 + \frac{L_a}{2} \tag{29}$$

$V_{\alpha x}$ is the voltage at the middle of the aperture paralleled to the x axis. K_a is the wave number of the aperture [19]. The magnetic current in the aperture parallel to x axis given by [16,17]:

$$M_{\alpha x} = -2\, E_{\alpha y} \tag{30}$$

The corresponding current density J_{mx} is given by:

$$J_{mx} = \frac{-2\, E_{\alpha y}}{h} \tag{31}$$

By substituting for J_{mx} from equation (31) into equation (26) the modes coefficients $\beta_{x,mn}$ are determined. Then the magnetic field H_x in the cavity is given by

$$H_x = \sum_{mn} A_{mn} \beta_{x,mn} K_n \cos(K_m x) \sin(K_n y) \tag{32}$$

3.1.3 Magnetic Field Component in y-direction

The eigenfunction expansion for the magnetic field component in y direction H_y is used for solving equation (21) [16];

$$H_y = \sum_{mn} \beta_{y,mn} \psi_{y,mn} \tag{33}$$

Figure 35 shows the aperture paralleled to y axis; the electric field distribution ($E_{\alpha x}$) can be determined using the following equations:

$$E_{\alpha x} = \frac{V_{\alpha y}}{W_a} \frac{\sin\left[K_a\left(\frac{L_a}{2} - (Y_2 - y)\right)\right]}{\sin\left(K_a \frac{L_a}{2}\right)} \qquad Y_2 - \frac{L_a}{2} \le y \le Y_2 \tag{34}$$

$$E_{\alpha x} = \frac{V_{\alpha y}}{W_a} \frac{\sin\left[K_a\left(\frac{L_a}{2} - (y - Y_2)\right)\right]}{\sin\left(K_a \frac{L_a}{2}\right)} \qquad Y_2 \le y \le Y_2 + \frac{L_a}{2} \tag{35}$$

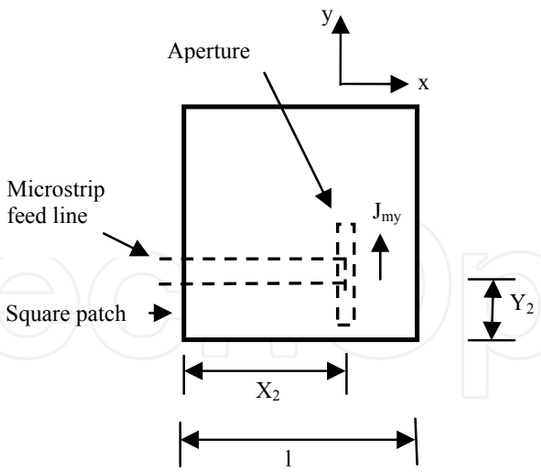


Fig. 35. Position of the aperture paralleled to *y*-axis

where V_{oy} is the voltage at the middle of the aperture paralleled to the *y* axis. The corresponding current density J_{my} is given by:

$$J_{my} = \frac{-2\,E_{ax}}{h} \tag{36}$$

The modes coefficients $\beta_{y,mn}$ are obtained by;

$$\beta_{y,mn} = \frac{j\omega\varepsilon}{(K_{mn}^2 - K^2)K_m^2} \int_0^{L_a} \int_0^{W_a} J_{my} . \psi_{y,mn}^* dx dy \tag{37}$$

The magnetic field H_y in the cavity is given by:

$$H_y = \sum_{mn} A_{mn} \beta_{y,mn} K_m \sin(K_m x) \cos(K_n y) \tag{38}$$

3.1.5 Input impedance

If the aperture is parallel to *x* direction; the admittance of the patch can be obtained by the following equation [16,20]:

$$Y_{x,ant} = \frac{\iiint_V H_x J_{mx} dV}{|E_z h|^2} \tag{39}$$

where *V* is the volume occupied by the source within which the magnetic currents exist. The electric field E_z inside the cavity is determined based on equation (13) and equation (15) as follows:

$$E_z = \frac{1}{j\omega\varepsilon}\left(\frac{\partial H_y}{\partial x} - \frac{\partial H_x}{\partial y}\right) \tag{40}$$

But the admittance of the patch in case of the aperture is parallel to *y* direction can be obtained from equation (41):

$$Y_{y,ant} = \frac{\iiint_V H_y J_{my} dV}{|E_z h|^2} \tag{41}$$

The admittance value of the aperture Y_{ap} can be obtained from the transmission line model of the aperture by considering the aperture as two short circuited slot lines [2].

$$Y_{ap} = \frac{-2j}{Z_{ca}} \cot(K_a \frac{L_a}{2}) \tag{42}$$

where Z_{ca}, L_a are, respectively, the characteristic impedance, the length of the aperture. The input impedance of the ACMSA is given by:

$$Z_{in} = \frac{n^2}{Y_{x,ant} + Y_{ap}} + \frac{n^2}{Y_{y,ant} + Y_{ap}} \tag{43}$$

The open microstrip stub line (L_{os}) which is used for forcing the imaginary part of the input impedance to be zero, is obtained by;

$$L_{os} = \frac{1}{K_F} \cot^{-1}\left(\frac{imaginary(Z_{in})}{2\,Z_F}\right) \tag{44}$$

The input impedance of the ACMSA with the open microstrip stub line is given by

$$Z_{in_stub} = \frac{n1^2}{Y_{x,ant} + Y_{ap}} + \frac{n1^2}{Y_{y,ant} + Y_{ap}} - 2jZ_F \cot(K_F L_{os}) \tag{45}$$

Z_F and K_F, are, respectively, the characteristic impedance and the wave number of the microstrip feed line; n1 is the transformation ratio which describes the coupling between the microstrip feed line and the patch [19].

3.2 Circular polarization diversity with ACMSA

The electric field components in *x*-direction (E_x) and y direction (E_y) are generated by putting an aperture parallel to *y* axis and *x* axis respectively as shown in Figure 36. The circular polarization diversity requires the phase shift between E_x and E_y to be $\pm 90^\circ$. By using the quadrature hybrid as a feeder for the square patch microstrip antenna the circular polarization diversity can be achieved. When the right port of the hybrid is selected, E_x will lead E_y by 90° and the RHCP will be generated. If the left port of the hybrid is selected, E_x will lag E_y by 90° and the LHCP will be generated [20].

3.3 Geometry of ACMSA

The geometry of the proposed ACMSA with a circularly polarized diversity is shown in Figure 37. The square patch is printed on Rogers's substrate (patch substrate) with a thickness h_t=0.85 mm, a loss tangent=0.0021 and a dielectric constant $\varepsilon_r = 3.55$. Based on the cavity model theory and ADS optimization the length of the square patch is 31.599 mm at a resonant frequency of 2.437 GHz. The quadrature hybrid is printed on the Roger's substrate

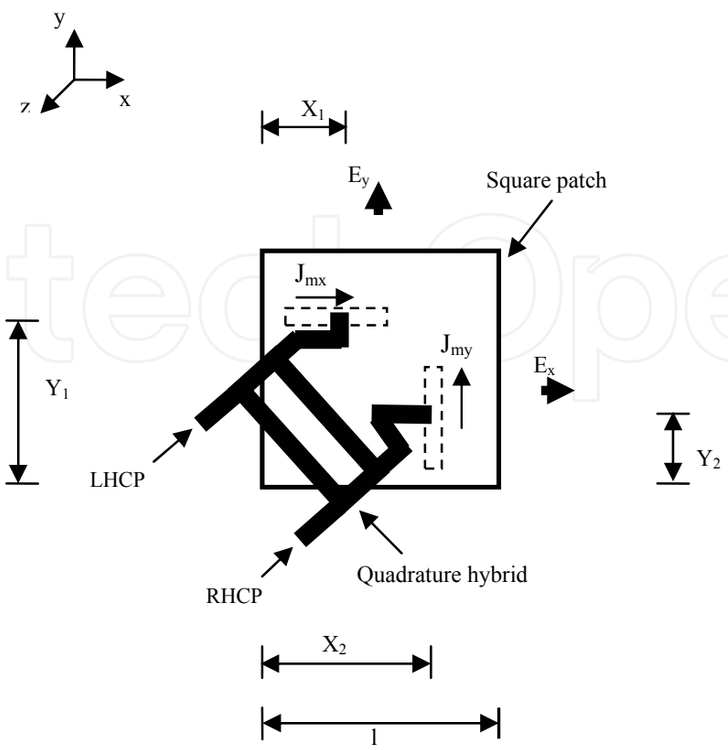


Fig. 36. Circular polarization diversity with ACMSA

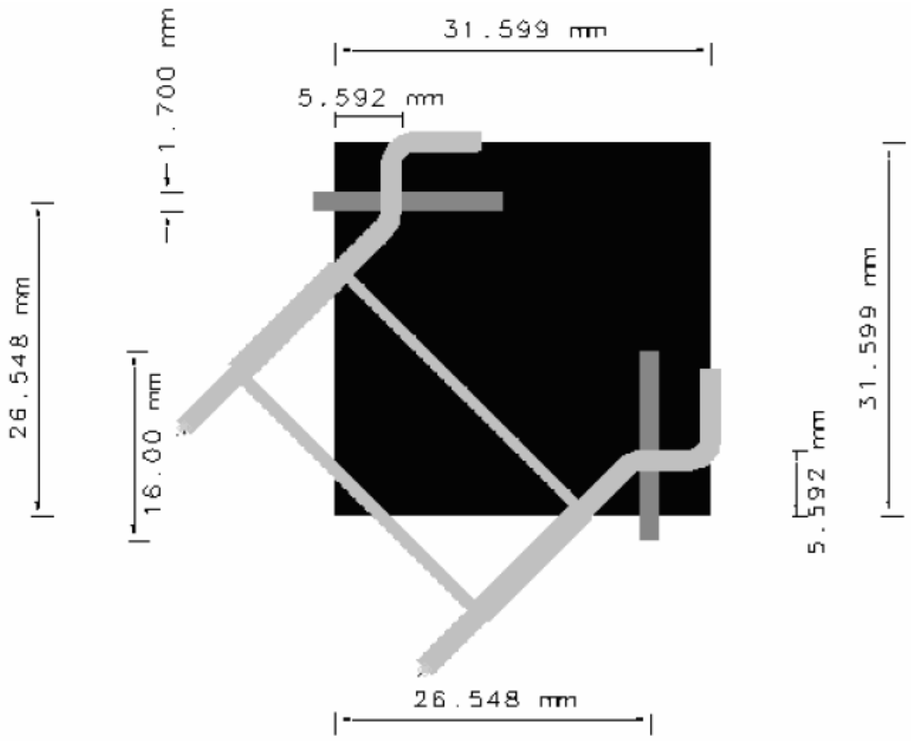


Fig. 37. Geometry of the proposed ACMSA

(feed substrate) which has the same parameters as those of the patch substrate. The ground plane exists in between the patch substrate and the feed substrate. There are two identical apertures printed on the ground plane, one parallel to x-axis and the other paralleled to y-axis. The length and the width of the aperture are 16 mm and 1.7 mm respectively [2, 14, 16-19, 21].

The size of the geometry with bended open microstrip stub line (L_{os}) as shown in Figure 37 is about 22% smaller than that of the other geometry shown in Figure 38 which has straight open microstrip stub line (L_{os}).

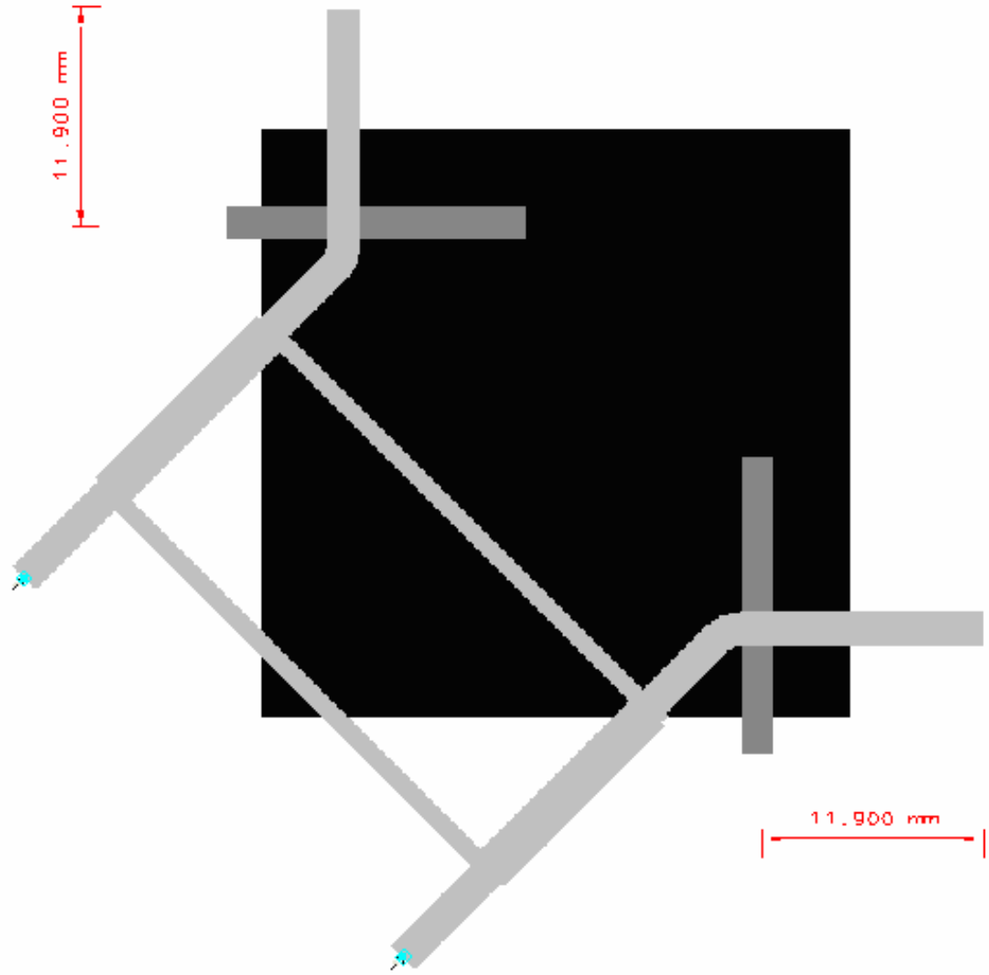


Fig. 38. Geometry of ACMSA with straight open microstrip stub line

The ADS is used to convert the straight L_{os} into its equivalent bended L_{os} by modeling the straight L_{os} using MLOC with length 11.9 mm in ADS schematic as shown in Figure 39. The ADS schematic as shown in Figure 40 is implemented to model the bended L_{os} using two MLIN of length 3 mm, MCURVE and MLOC with variable length.

The ADS schematic as shown in Figure 41 is used to find the optimum length of the bended L_{os}.

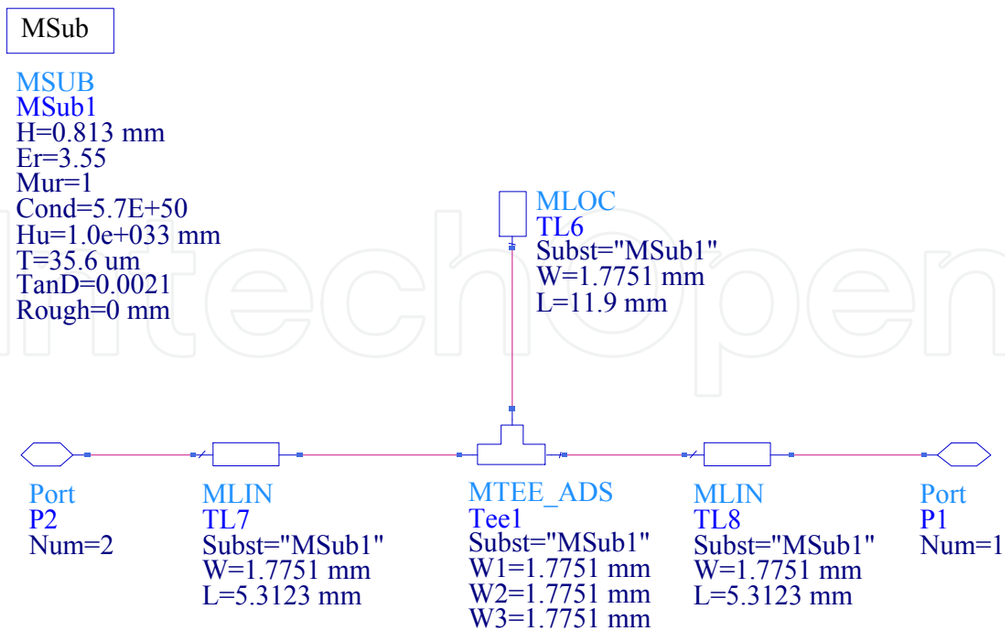


Fig. 39. ADS schematic model for straight open microstrip stub line

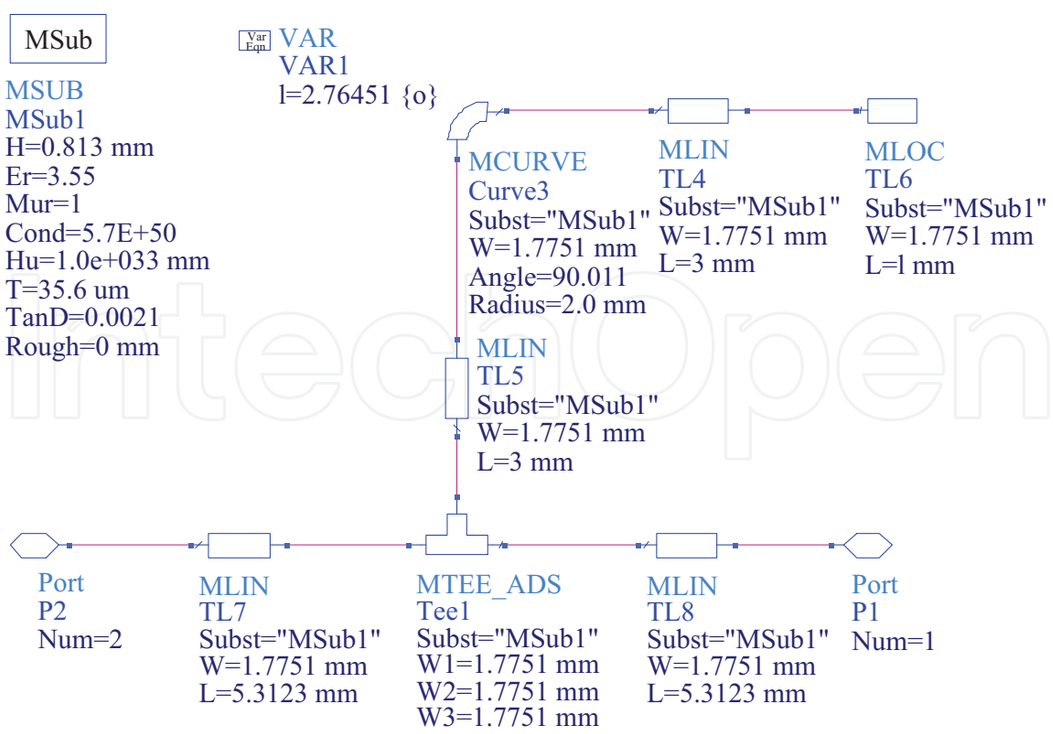


Fig. 40. ADS schematic model for bended open microstrip stub line

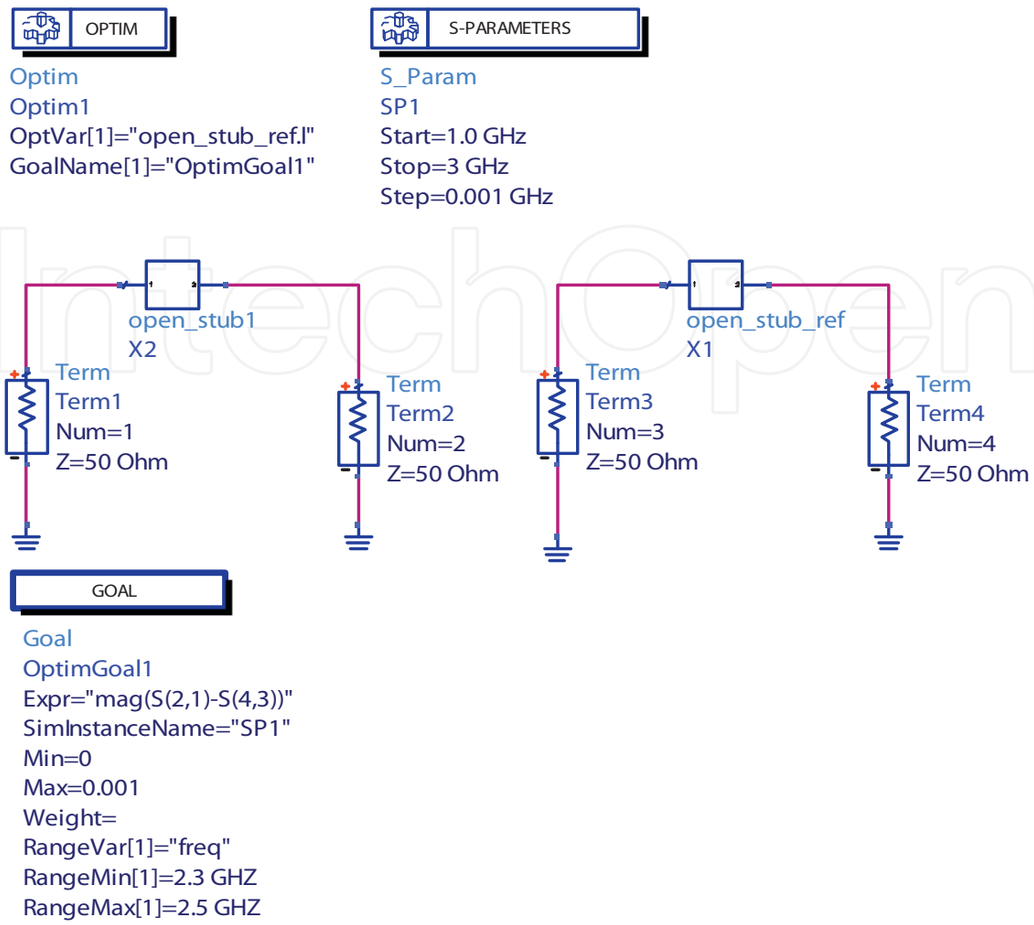


Fig. 41. ADS schematic to find the optimum length of the bended open microstrip stub line

Figure 42 shows that the bended L_{os} is equivalent to straight L_{os} when the variable length is 2.76451 mm.

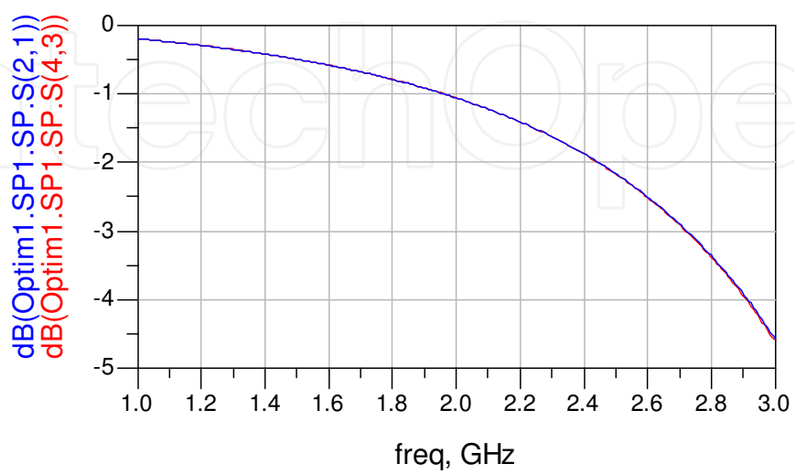


Fig. 42. Simulated responses for straight and bended open microstrip stub line

3.4 Simulation and measured results

The value of Y_1 and X_2 is the same which is selected as 26.548 mm to place the quadrature hybrid at a further distance into the square patch in order to minimize the size of the ACMSA. The value of X_1 and Y_2 is the same and equals to the distance at which the real part of the input impedance is approached to 50 Ω at the center of each aperture. Figure 43 shows the input impedance of the ACMSA without the implementation of the open microstrip stub line (L_{os}). In this case the imaginary part of the input impedance is 42.86 Ω when X_1 is 5.688 mm. The length of the open microstrip stub line is determined in order to force the imaginary part of input impedance to be zero.

Figure 44 shows the input impedance of the ACMSA with L_{os} equals to 11.9 mm. The results for X_1, X_2, Y_1 and Y_2 are obtained using the Matlab simulation and these results are optimized using ADS as shown in Figure 37.

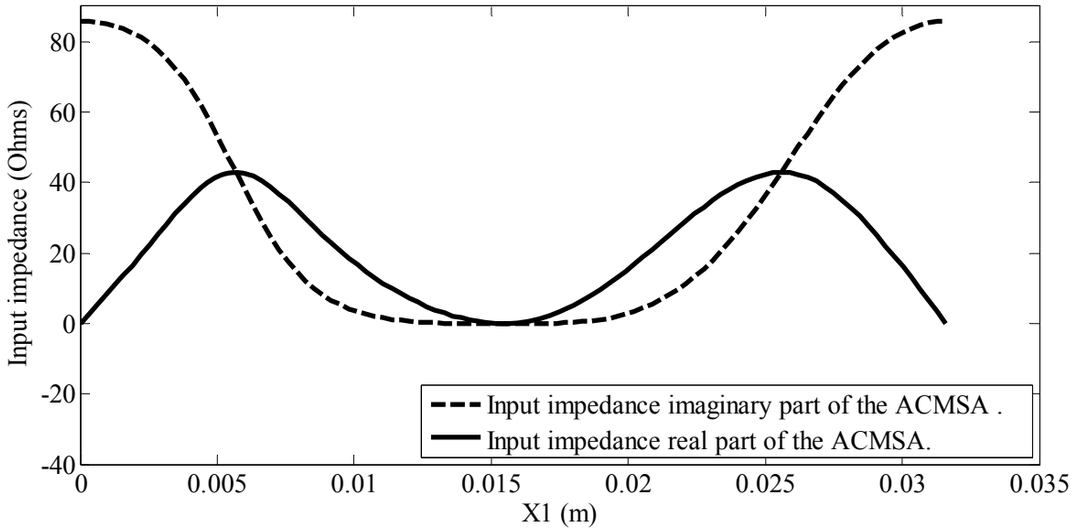


Fig. 43. Simulated input impedance of the ACMSA without L_{os}

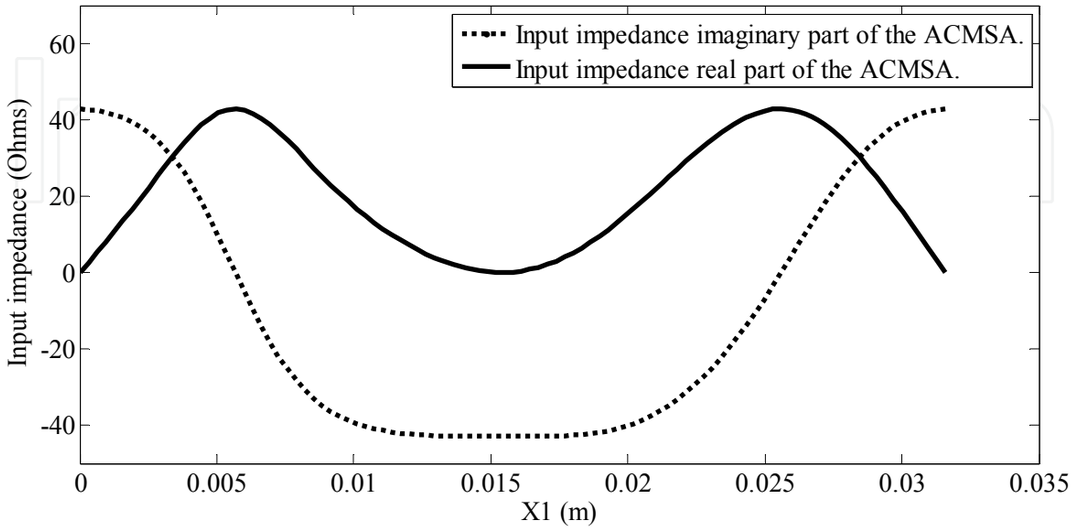


Fig. 44. Simulated input impedance of the ACMSA with L_{os}

If the right port of the quadrature hybrid is selected, the reflection coefficient (S_{11}) versus the frequency and the normalized measured radiation pattern of the ACMSA are shown in Figures 45 and 46 respectively. Figure 45 shows that, the proposed ACMSA provides an impedance bandwidth of 20.1% at port 1 (for S_{11} < -10dB).

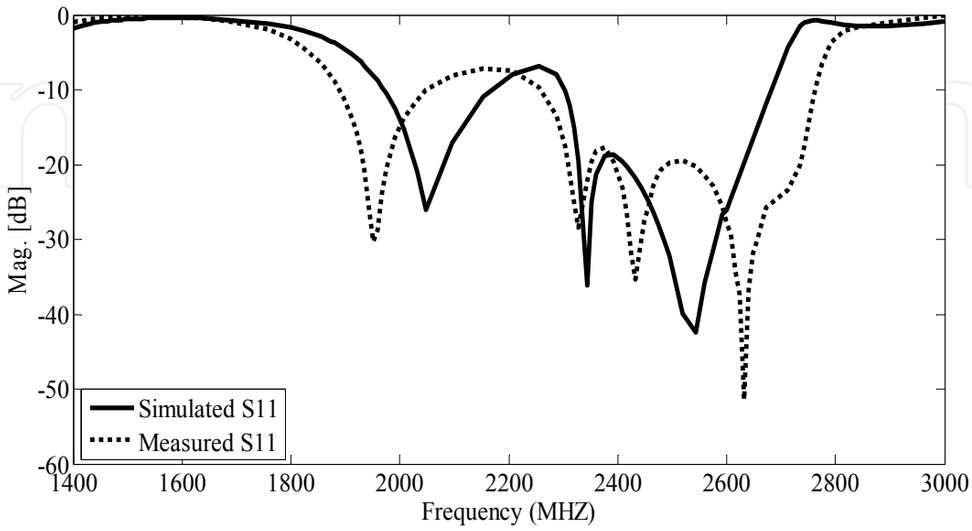


Fig. 45. Reflection coefficient versus frequency when the right port of the quadrature hybrid is selected

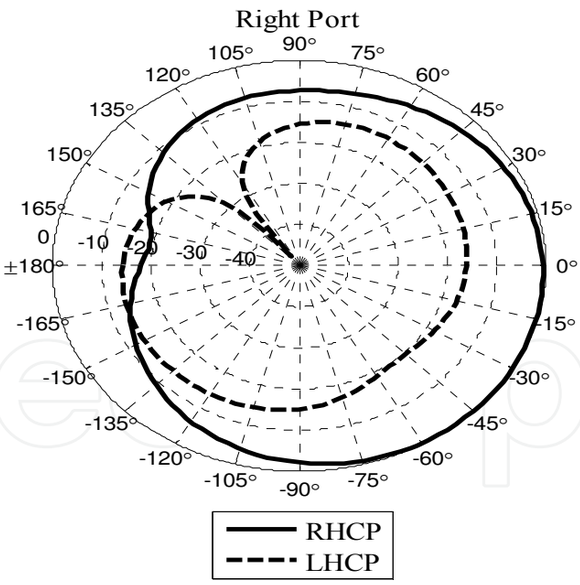


Fig. 46. Normalized measured radiation pattern when the right port of the quadrature hybrid is selected

Figures 47 and 48 respectively show the reflection coefficient (S_{22}) versus the frequency and the normalized measured radiation pattern of the ACMSA, when the left port of the quadrature hybrid is selected. The impedance bandwidth of 20 % is obtained at port 2 (for S_{22} < -10dB) as evident from Figure 47.

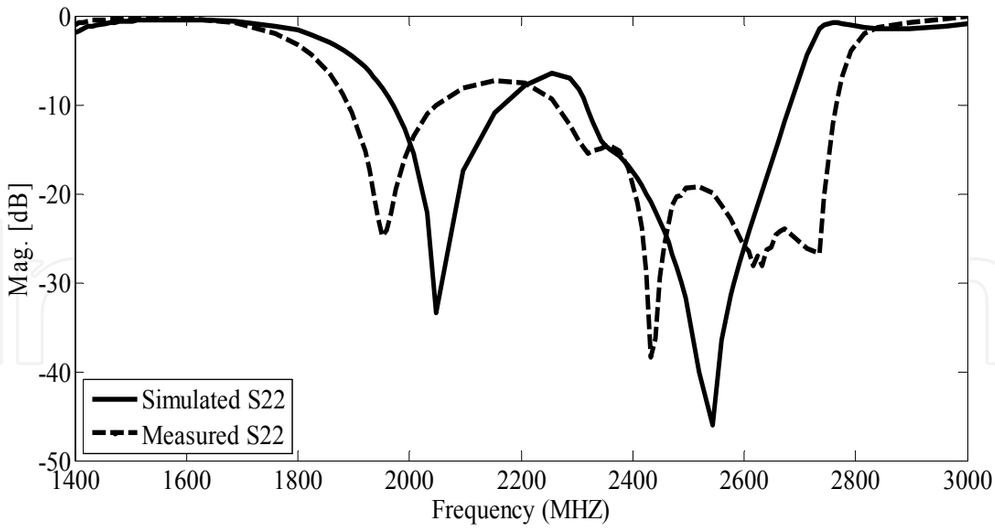


Fig. 47. Reflection coefficient versus frequency when the left port of the quadrature hybrid is selected

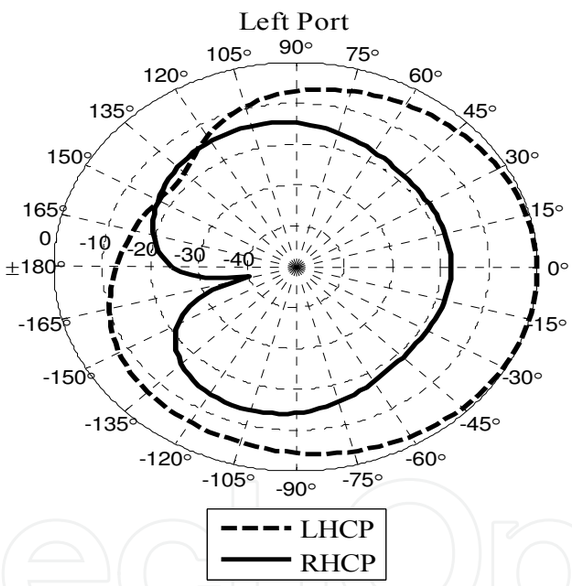


Fig. 48. Normalized measured radiation pattern when the left port of the quadrature hybrid is selected

The fabrication of one ACMSA requires two substrate slices (patch substrate and feed substrate). The parameters setup in ADS Momentum for substrate layers is shown in Figure 49.

The top side and the bottom side of each substrate are covered by metal layer. Parameters setup in ADS Momentum for metallization layers is shown in Figure 50. For patch substrate, the square patch is printed on the top side while the metal layer on the bottom side is removed. For the feed substrate the quadrature hybrid is printed on the bottom side while the two apertures are etched on the top side which is considered as a ground plane.

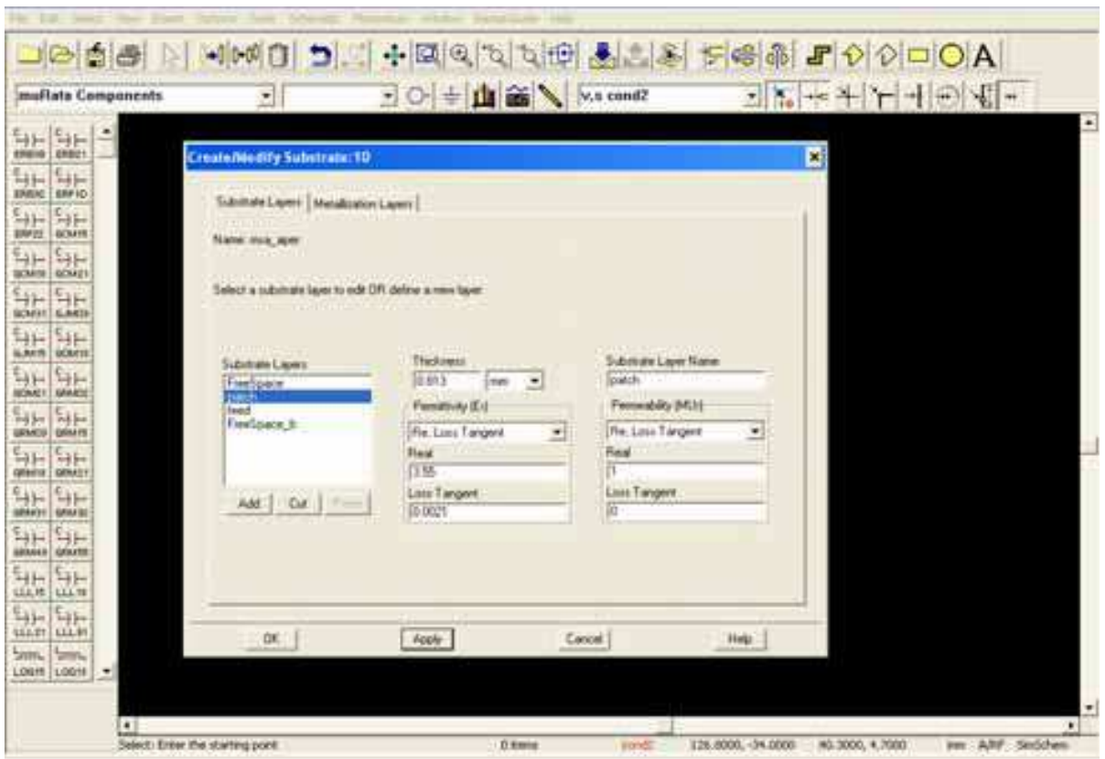


Fig. 49. Parameters setup in ADS Momentum for substrate layers of the ACMSA

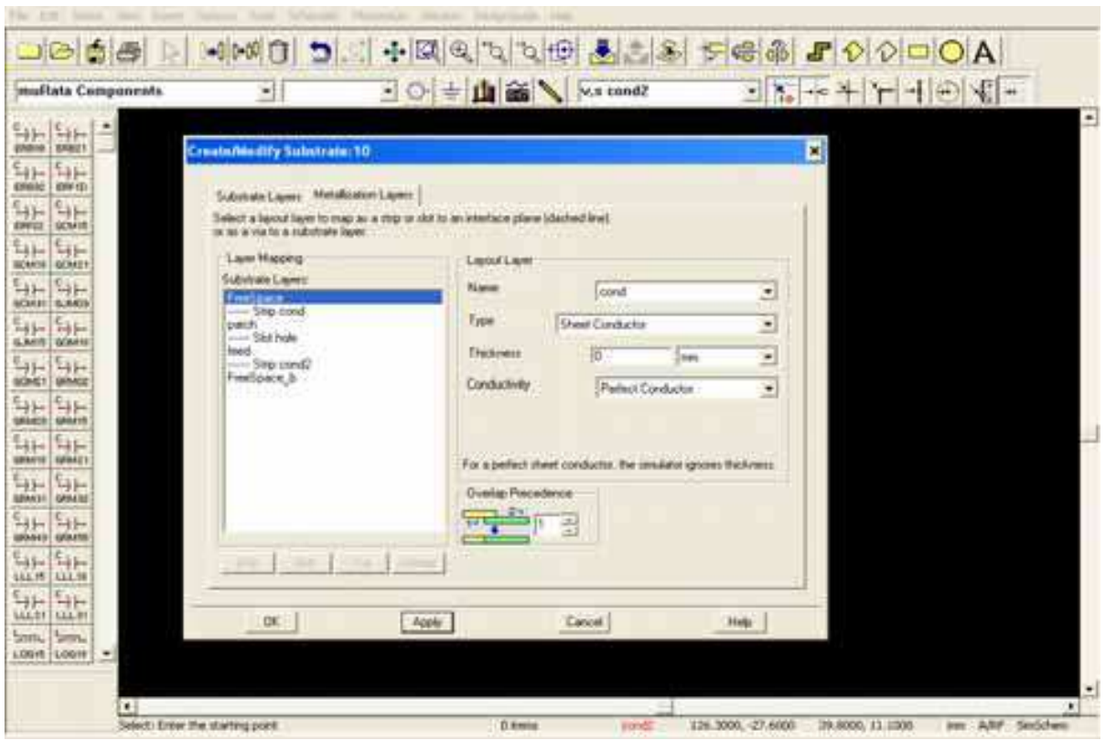


Fig. 50. Parameters setup in ADS Momentum for metallization layers of ACMSA

Figures 51 and 52 respectively show the fabricated patch substrate and feed substrate of the ACMSA.



Fig. 51. Fabricated patch substrate

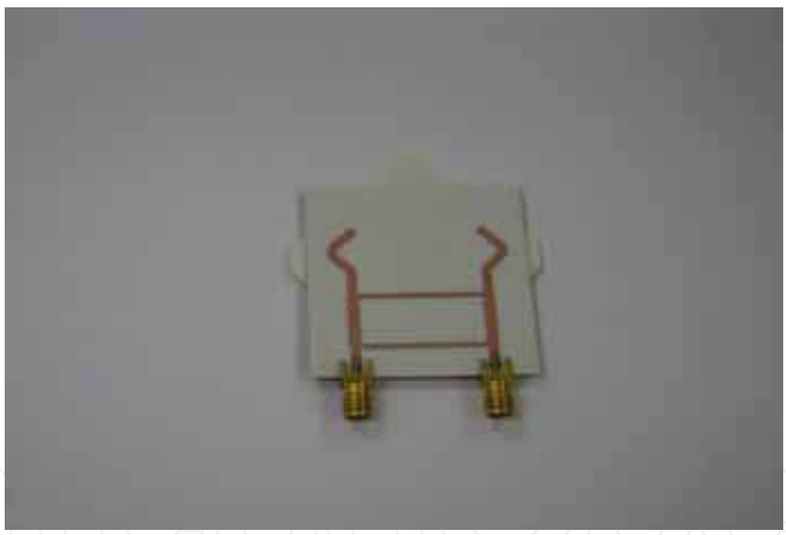


Fig. 52. Fabricated feed substrate

The measured gain at 2.437 GHz for right port and left port are 5dBi and 4.6 dBi respectively. The gain for the left port is measured using left hand circularly polarized standard antenna (2.4 GHz, 8 dBi, LHCP, Flat Patch Antenna), while the gain for the right port is measured using right hand circularly polarized standard antenna (2.4 GHz, 8dBi, RHCP, Flat Patch Antenna). Figure 53 shows the measured axial ratio at both ports of the ACMSA.

The ACMSA produces two beams, one of which is RHCP and the other is LHCP as shown in Figures 46 and 48 respectively. The axial ratio and the radiation pattern are measured in Satimo chamber. The measurement system consists of probe antennas mounted with equal spacing on a circular arch as shown in Figure 54. The measured data is collected automatically and saved in MS Excel format.

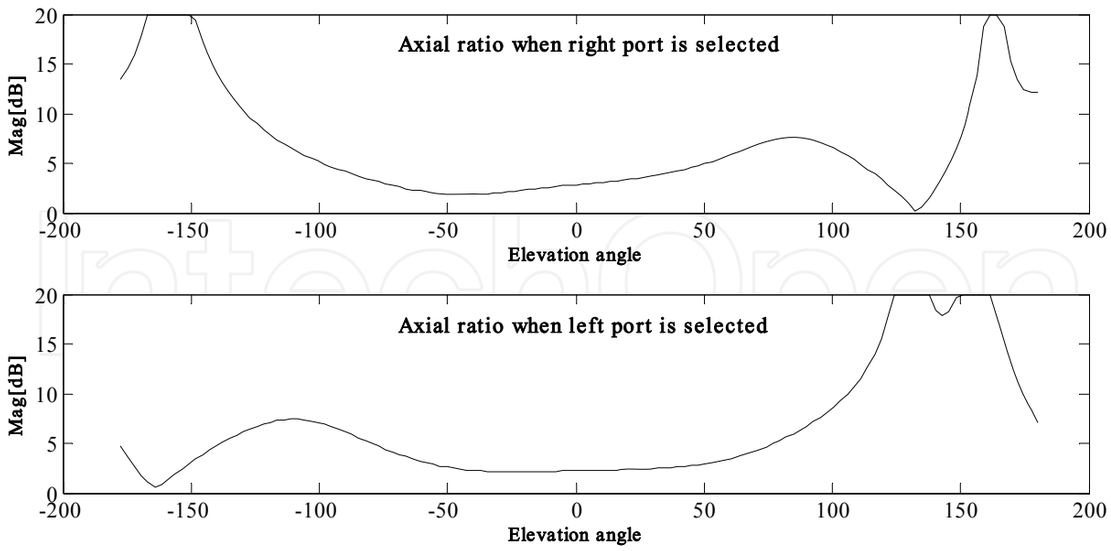


Fig. 53. Measured axial ratio at both ports of the ACMSA versus an elevation angle

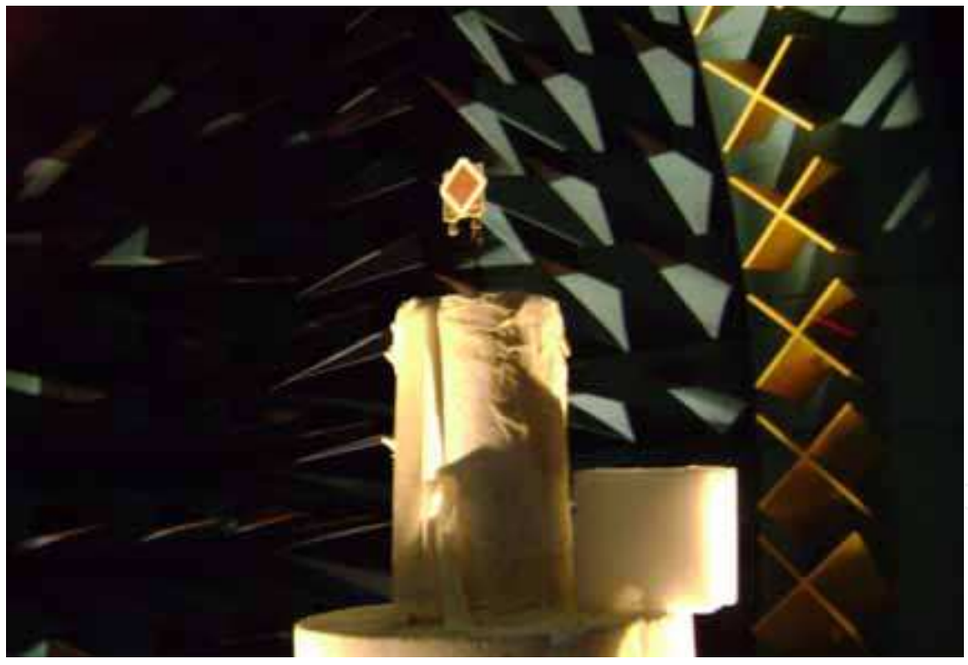


Fig. 54. Measuring aperture-coupled microstrip antenna inside Satimo chamber

The size of the ACMSA is much smaller than that of the microstrip antenna which is fed by a quadrature hybrid without using an aperture coupled structure. The utilization of the aperture coupled structure could reduce the antenna size substantially compared with the one without aperture coupled structure. For instance, size reductions of 72% and 60 % are achieved compared to the cases of [22] and [23] respectively. The proposed ACMSA has a better bandwidth and good axial ratio compared to the designs presented by [22, 24-26]. Further, it can receive the RHCP and the LHCP simultaneously whereas the reconfigurable

patch antennas could receive only one polarization type at a time [22, 24-26]. Above all, the proposed geometry can provide circular polarization diversity with good axial ratio over a broad angular range, wide bandwidth and small size.

4. Conclusions

A circularly polarized microstrip antenna array could be generated with linearly polarized patches. The separation distance between the patches in the *x*-direction has a strong effect on the *E*-plane of the planar microstrip antenna array pattern, whereas the separation distance between the patches in the *y*-direction has a weak affect on the *H*-plane of the planar microstrip antenna array pattern. Four narrow beams at four different directions are obtained through the excitation of a planar microstrip antenna array by a 4×4 Butler matrix. These four beams possess circular polarization diversity, good axial ratio and high gain.
Circular polarization diversity could be generated by coupling the quadrature hybrid to the square patch through two apertures. The aperture coupled structure minimized the size of the microstrip antenna which is fed by the quadrature hybrid. The proposed geometry provides good axial ratio over a broad angular range and wide bandwidth. The analysis of the ACMSA using the cavity model is comparable with the full-wave analysis and the experimental results.

APPENDIX A

ADS schematics to design path 3 and path 4 of the planar microstrip antenna array with 4×4 Butler matrix

Figure A.1 shows the ADS schematic for path 3 which connects between antenna 3 and 4×4 Butler matrix. The ADS schematic to modify the length of path 3 is shown in Figure A.2.

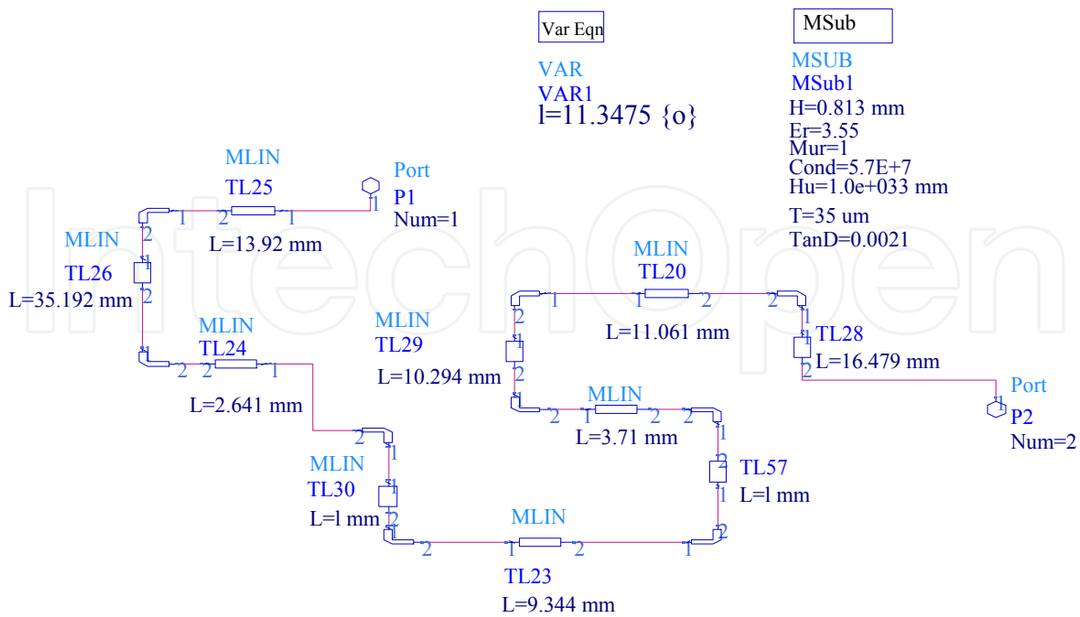


Fig. A.1 ADS schematic for path 3

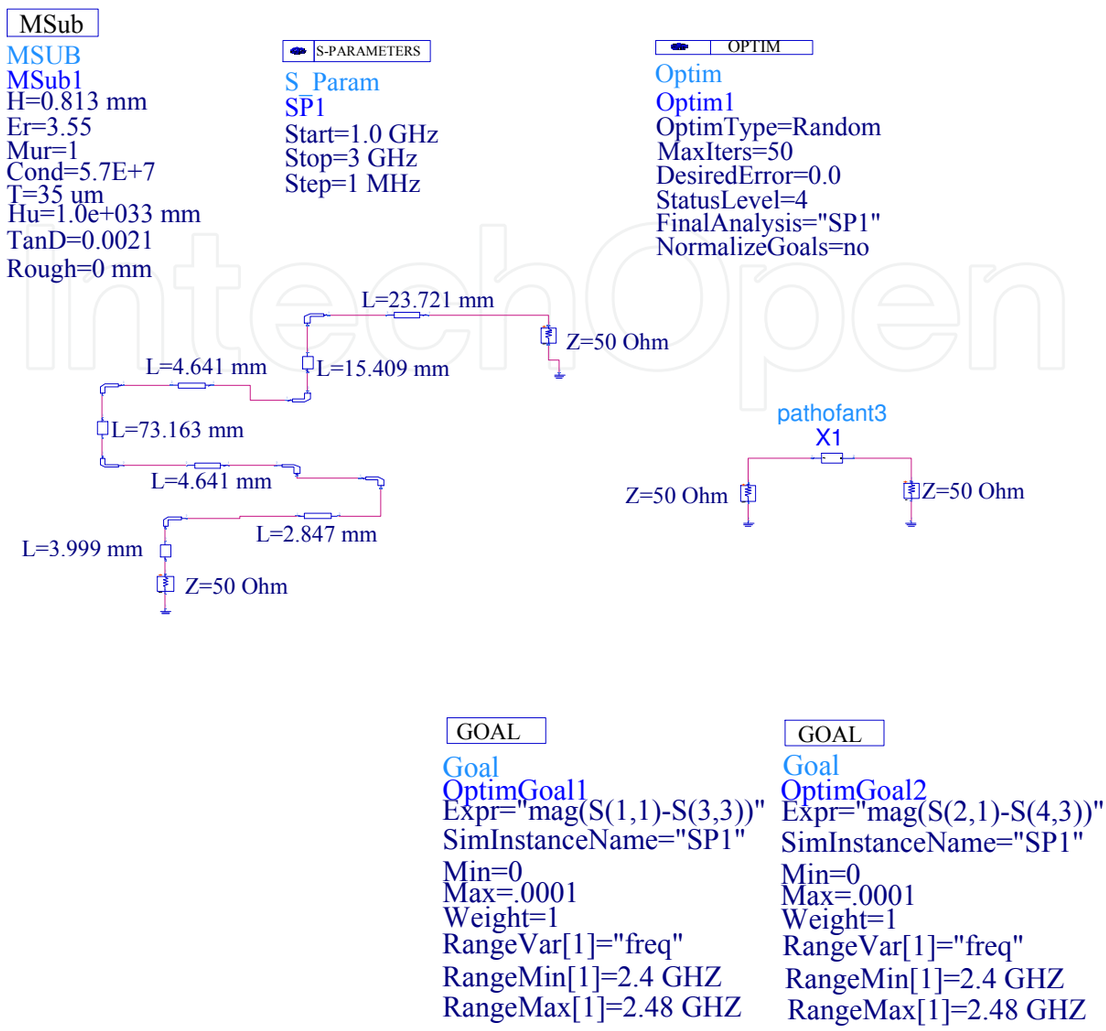


Fig. A.2 ADS schematic to modify the length of path 3

The ADS simulated results for phases of path 3 and reference path are shown in Figure A.3.

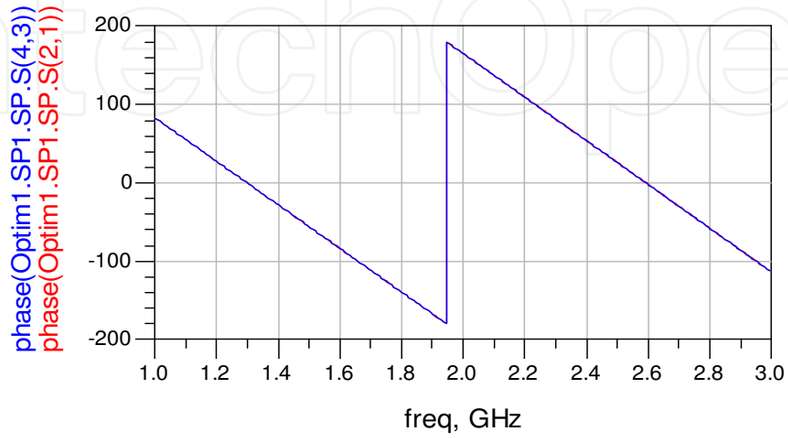


Fig. A.3 ADS simulated results for phases of path 3 and reference path

The ADS schematic for path 4 which connects between antenna 4 and 4×4 Butler matrix is shown in Figure A.4.

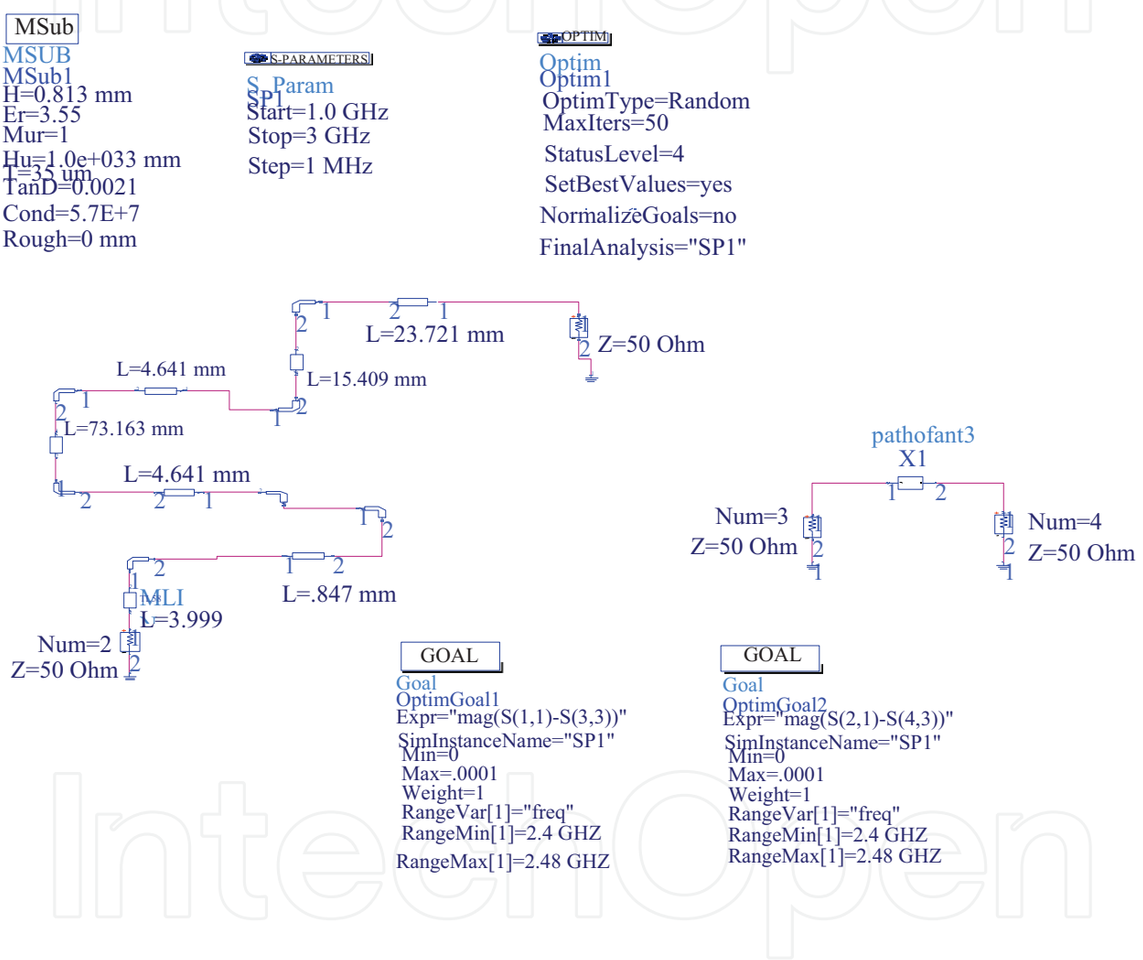


Fig. A.4 ADS schematic for modifying length of the path connecting antenna 4 and 4×4 Butler matrix

The length of the path 4 is modified by using the ADS schematic shown in Figure A.5. The ADS simulated results for phases of path 4 and reference path are shown in Figure A.6.

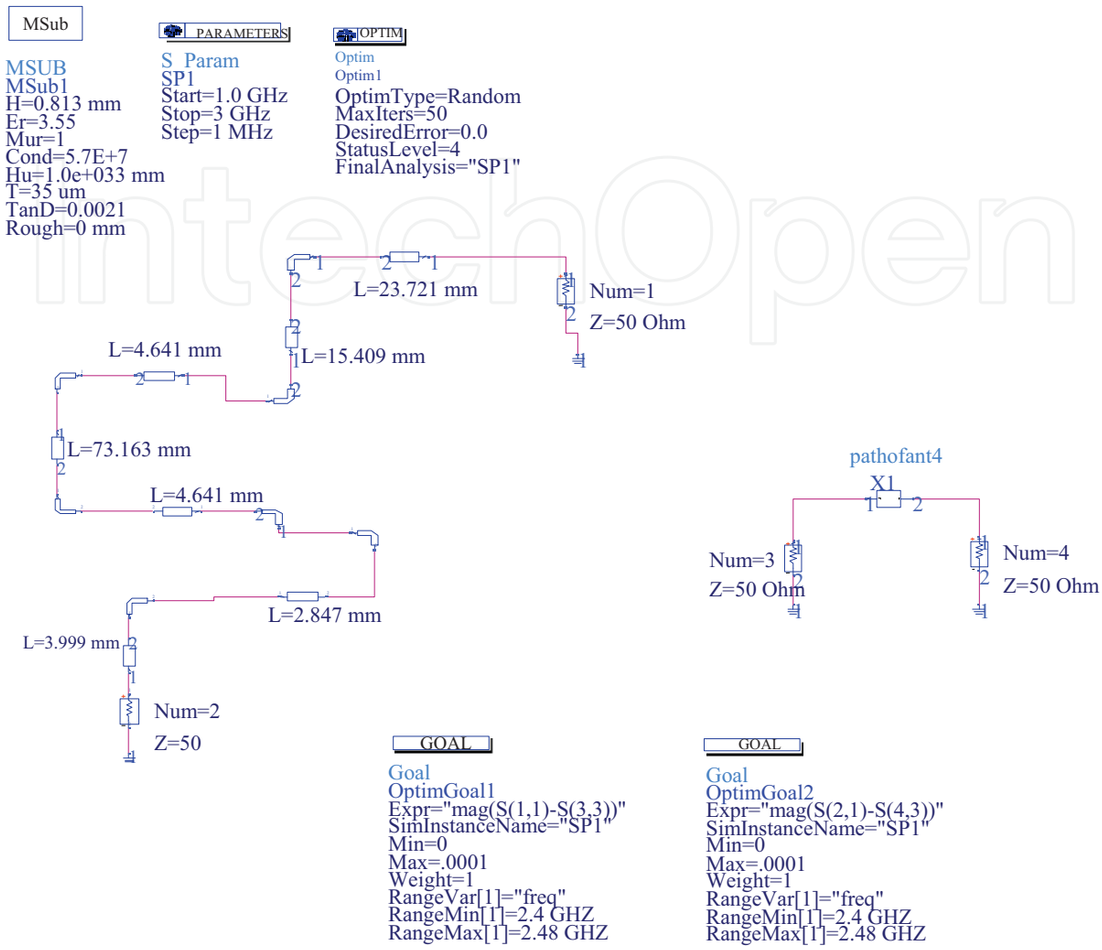


Fig. A.5 ADS schematic to modify the length of path 4

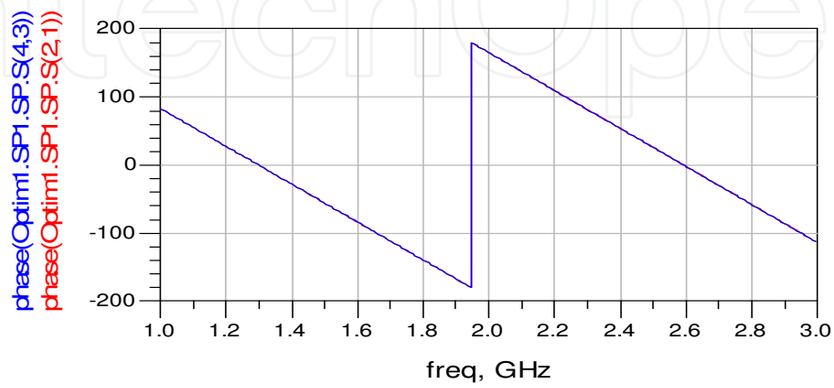


Fig. A.6 ADS simulated results for phases of path 4 and reference path

APPENDIX B

Propagation constant inside the cavity

$$\frac{\partial^2 \psi_{y,mn}}{\partial x \partial y} - \frac{\partial^2 \psi_{x,mn}}{\partial y^2} - K_{mn}^2 \psi_{x,mn} = 0 \tag{B.1}$$

$$\psi_{x,mn} = A_{mn} K_n \cos(K_m x) \sin(K_n y) \tag{B.2}$$

$$\psi_{y,mn} = -A_{mn} K_m \cos(K_n y) \sin(K_m x) \tag{B.3}$$

where $A_{mn} = \frac{\chi_{mn}}{\sqrt{\varepsilon . l^2 . h_t}}$

$$\chi_{mn} = \begin{cases} 1, & m = 0 \; and \; n = 0 \\ \sqrt{2}, & m = 0 \; or \; n = 0 \\ 2, & m \neq 0 \; and \; n \neq 0 \end{cases}$$

For a non radiating cavity

$$K_m = \frac{m\pi}{l}, K_n = \frac{n\pi}{l} \tag{B.4}$$

$$\frac{\partial \psi_{y,mn}}{\partial x} = -A_{mn} K_m^2 \cos(K_n y) \cos(K_m x) \tag{B.5}$$

$$\frac{\partial^2 \psi_{y,mn}}{\partial x \partial y} = A_{mn} K_m^2 K_n \sin(K_n y) \cos(K_m x) \tag{B.6}$$

$$\frac{\partial \psi_{x,mn}}{\partial y} = A_{mn} K_n^2 \cos(K_m x) \cos(K_n y) \tag{B.7}$$

$$\frac{\partial^2 \psi_{x,mn}}{\partial y^2} = -A_{mn} K_n^3 \cos(K_m x) \sin(K_n y) \tag{B.8}$$

$$A_{mn} K_m^2 K_n \sin(K_n y) \cos(K_m x) + A_{mn} K_n^3 \sin(K_n y) \cos(K_m x) = K_{mn}^2 A_{mn} K_n \sin(K_n y) \cos(K_m x) \tag{B.9}$$

$$K_{mn}^2 = K_m^2 + K_n^2 \tag{B.10}$$

APPENDIX C

Mode coefficients in *x*-direxion inside the cavity

$$\frac{\partial^2 H_y}{\partial x \partial y} = \sum_{mn} \beta_{y,mn} \frac{\partial^2 \psi_{y,mn}}{\partial x \partial y} \tag{C.1}$$

$$\frac{\partial^2 H_x}{\partial y^2} = \sum_{mn} \beta_{x,mn} \frac{\partial^2 \psi_{x,mn}}{\partial y^2} \tag{C.2}$$

By substituting from equation (C.1) and (C.2) into equation (20) the following equation is obtained:

$$\sum_{mn} \beta_{y,mn} \frac{\partial^2 \psi_{y,mn}}{\partial x \partial y} - \sum_{mn} \beta_{x,mn} \frac{\partial^2 \psi_{x,mn}}{\partial y^2} - K^2 \sum_{mn} \beta_{x,mn} \psi_{x,mn} = j\omega\varepsilon J_{mx} \tag{C.3}$$

$$\frac{\partial^2 \psi_{y,mn}}{\partial x \partial y} - \frac{\partial^2 \psi_{x,mn}}{\partial y^2} = K_{mn}^2 \psi_{x,mn} \tag{C.4}$$

$$\sum_{mn} \beta_{y,mn} = \sum_{mn} \beta_{x,mn} \tag{C.5}$$

By substituting from equations (C.4) and (C.5) into equation (C.3) the equation (C.6) is obtained:

$$\sum_{mn} \beta_{x,mn} K_{mn}^2 \psi_{x,mn} - \sum_{mn} \beta_{x,mn} K^2 \psi_{x,mn} = j\omega\varepsilon J_{mx} \tag{C.6}$$

$$\sum_{mn} \beta_{x,mn} (K_{mn}^2 - K^2) \int_0^l \int_0^l \psi_{x,mn} . \psi_{x,mn}^* dxdy = j\omega\varepsilon \int_0^{W_a} \int_0^{L_a} J_{mx} . \psi_{x,mn}^* dxdy \tag{C.7}$$

Where $\psi_{x,mn}^*$ is the complex conjugate of $\psi_{x,mn}$

$$\int_0^l \int_0^l \psi_{x,mn} . \psi_{x,mn}^* dxdy = K_n^2 \tag{C.8}$$

5. References

[1] L. Basilio, M. Khayat, J. Williams, and S. Long, "The dependence of the input impedance on feed position of probe and microstrip line-fed patch antennas," *IEEE Transactions on Antennas and Propagation*, vol. 49, pp. 45-47, 2001.

[2] M. Mathian, E. Korolkewicz, P. Gale, and E. Lim, "Design of a circularly polarized 2x2 patch array operating in the 2.45 GHZ ISM band," *Microwave Journal*, vol. 45, pp. 280-286, 2002.

[3] T. Denidni and T. Libar, "Wide band four-port butler matrix for switched multibeam antenna arrays," in *14th IEEE Proceedings on Personal, Indoor and Mobile Radio Communications*. vol. 3, 2003, pp. 2461-2464.

[4] G. Srivastava and V. Gupta, "Microwave devices and circuit design," New Delhi: Prentice-Hall of India, 2006, p. 339.

[5] N. Jean-Sébastien and D. Gilles, "Microstrip EHF Butler matrix design and realization," *ETRI Journal*,, vol. 27, pp. 788-797, 2005.

[6] M. Halim, "Adaptive array measurements in communications," Boston: Artech House, 2001, pp. 170-177.

[7] J. Huang, "A technique for an array to generate circular polarization with linearly polarized elements," *IEEE Transactions on Antennas and Propagation*, vol. 34, pp. 1113-1124., 1986.
[8] J. Huang, "C.P. microstrip array with wide axial ratio bandwidth and single feed L.P. elements," in *International Symposium on Antennas and Propagation*. vol. 23, 1985, pp. 705-708.
[9] A. Rudge, "The handbook of antenna design. Vol.1," in *IEE electromagnetic waves series, 15* London: Peregrinus on behalf of the Institution of Electrical Engineers, 1982, pp. 1-29.
[10] K. Chang, "RF and microwave wireless systems," New York: Wiley, 2000, pp. 98-105.
[11] L. Johan, "Design and analysis of an electrically steerable microstrip antenna for ground to air use," in *Computer Science and Electrical Engineering*. vol. MSc: Luleå University of Technology, 2002.
[12] W. Ismail, "Active integrated antenna (AIA) with image rejection," in *Electrical and Computer Engineering*. vol. PhD: University of Birmingham, 2003.
[13] L. Ronglin, B. Pan, J. Laskar, and M. Tentzeris, "A novel low-profile broadband dual-frequency planar antenna for wireless handsets," *IEEE Transactions on Antennas and Propagation*, vol. 56, pp. 1155-1162, 2008.
[14] K. Carver and J. Mink, "Microstrip antenna technology," *IEEE Transactions on Antennas and Propagation*, vol. 29, pp. 2-24, 1981.
[15] H. John and J. Encinar, "Reflectarray antennas," Piscataway, N.J.; Hoboken, N.J.: IEEE Press ; Wiley-Interscience, 2008, p. 143.
[16] B. Al-Jibouri, H. Evans, E. Korolkiewicz, E. Lim, A. Sambell, and T. Viasits, "Cavity model of circularly polarised cross-aperture-coupled microstrip antenna," *IEE Proceedings -Microwaves, Antennas and Propagation*, vol. 148, pp. 147-152, 2001.
[17] S. Kanamaluru, L. Ming-Yi, and C. Kai, "Analysis and design of aperture-coupled microstrip patch antennas and arrays fed by dielectric image line," *IEEE Transactions on Antennas and Propagation*, vol. 44, pp. 964-974, 1996.
[18] M. Himdi, J. Daniel, and C. Terret, "Analysis of aperture-coupled microstrip antenna using cavity method," *Electronics Letters*, vol. 25, pp. 391-392, 1989.
[19] R. Garg, "Microstrip antenna design handbook," Boston, MA: Artech House, 2001, pp. 542,786-788.
[20] A. Petosa, "Dielectric resonator antenna handbook," in *Artech House antennas and propagation library* Boston: Artech House, 2007, pp. 49-50, 171-178.
[21] G. Parker, "A dual polarized microstrip ring antenna with very good isolation," in *Electrical Engineering*. vol. MSc: Kingston Ontario: Royal Military College, 1997.
[22] G. Wu, W. Mu, G. Zhao, and Y. Jiao, "A novel design of dual circularly polarized antenna eed by L-strip," *Progress In Electromagnetics Research*, vol. PIER pp. 39-46, 2008.
[23] Z. Harith, "Design of a circular polarization microstrip antenna at 2.4GHZ," in *Electronics and Telecommunication,*. vol. MSc: Universiti Teknologi Malaysia, 2005.
[24] K. Chung, Y. Nam, T. Yun, and J. Choi, "Reconfigurable microstrip patch antenna with switchable polarization," *ETRI*, vol. 28, pp. 379-382, 2006.
[25] Y. Sung, T. Jang, and Y. Kim, "A reconfigurable microstrip antenna for switchable polarization," *IEEE Microwave and Wireless Components Letters*, vol. 14, pp. 534-536, 2004.
[26] Y. Fan and Y. Rahmat-Samii, "A reconfigurable patch antenna using switchable slots for circular polarization diversity," *IEEE Microwave and Wireless Components Letters*, vol. 12, pp. 96-98, 2002.



Microstrip Antennas

Edited by Prof. Nasimuddin Nasimuddin

ISBN 978-953-307-247-0
Hard cover, 540 pages
Publisher InTech
Published online 04, April, 2011
Published in print edition April, 2011

In the last 40 years, the microstrip antenna has been developed for many communication systems such as radars, sensors, wireless, satellite, broadcasting, ultra-wideband, radio frequency identifications (RFIDs), reader devices etc. The progress in modern wireless communication systems has dramatically increased the demand for microstrip antennas. In this book some recent advances in microstrip antennas are presented.

How to reference

In order to correctly reference this scholarly work, feel free to copy and paste the following:

Mohamed Elhefnawy and Widad Ismail (2011). Microstrip Antennas for Indoor Wireless Dynamic Environments, Microstrip Antennas, Prof. Nasimuddin Nasimuddin (Ed.), ISBN: 978-953-307-247-0, InTech, Available from: http://www.intechopen.com/books/microstrip-antennas/microstrip-antennas-for-indoor-wireless-dynamic-environments

INTECH
open science | open minds

InTech Europe
University Campus STeP Ri
Slavka Krautzeka 83/A
51000 Rijeka, Croatia
Phone: +385 (51) 770 447
Fax: +385 (51) 686 166
www.intechopen.com

InTech China
Unit 405, Office Block, Hotel Equatorial Shanghai
No.65, Yan An Road (West), Shanghai, 200040, China
中国上海市延安西路65号上海国际贵都大饭店办公楼405单元
Phone: +86-21-62489820
Fax: +86-21-62489821

© 2011 The Author(s). Licensee IntechOpen. This chapter is distributed under the terms of the Creative Commons Attribution-NonCommercial-ShareAlike-3.0 License, which permits use, distribution and reproduction for non-commercial purposes, provided the original is properly cited and derivative works building on this content are distributed under the same license.

IntechOpen

IntechOpen